The Emirates Exploration Imager (EXI) Instrument on the Emirates Mars Mission (EMM) Hope Mission

A.R. Jones[1] · M. Wolff[2] · M. Alshamsi[3] · M. Osterloo[2] · P. Bay[1] · N. Brennan[1] · K. Bryant[1] ·
Z. Castleman[1] · A. Curtin[1] · E. DeVito[1] · V.A. Drake[1] · D. Ebuen[1] · J. Espejo[1] · J. Farren[1] ·
B. Fenton[1] · C. Fisher[1] · M. Fisher[1] · K. Fortier[1] · S. Gerwig[1] · B. Heberlein[1] ·
C. Jeppesen[1] · M.A. Khoory[3] · S. Knappmiller[1] · J. Knavel[1] · K. Koski[1] · K. Looney[1] ·
P. Lujan[1] · M. Miller[1] · G. Newcomb[1] · G. Otzinger[1] · H. Passe[1] · E. Pilinski[1] · H. Reed[1] ·
R. Shuping[2] · P. Sicken[1] · D. Summers[1] · S. Wade[1] · L. Walton[1] · J.L. Yaptengco[1]

Abstract

The Emirates Exploration Imager (EXI) on-board the Emirates Mars Mission (EMM) offers both regional and global imaging capabilities for studies of the Martian atmosphere. EXI is a framing camera with a field-of-view (FOV) that will easily capture the martian disk at the EMM science orbit periapsis. EXI provides 6 bandpasses nominally centered on 220, 260, 320, 437, 546, 635 nm using two telescopes (ultraviolet (UV) and visible(VIS)) with separate optics and detectors. Images of the full-disk are acquired with a resolution of 2–4 km per pixel, where the variation is driven by periapsis and apoapsis points of the orbit, respectively. By combining multiple observations within an orbit with planetary rotation, EXI is able to provide diurnal sampling over most of the planet on the scale of 10 days. As a result, the EXI dataset allows for the delineation of diurnal and seasonal timescales in the behavior of atmospheric constituents such as water ice clouds and ozone.

This combination of temporal and spatial distinguishes EXI from somewhat similar imaging systems, including the Mars Color Imager (MARCI) onboard the Mars Reconnaissance Orbiter (MRO) (Malin et al. in Icarus 194(2):501–512, 2008) and the various cameras on-board the Hubble Space Telescope (HST; *e.g.,* James et al. in J. Geophys. Res. 101(E8):18,883–18,890, 1996; Wolff et al. in J. Geophys. Res. 104(E4):9027–9042, 1999). The former, which has comparable spatial and spectral coverage, possesses a limited local time view (e.g., mid-afternoon). The latter, which provides full-disk imaging, has limited spatial resolution through most of the Martian year and is only able to provide (at most) a few observations per year given its role as a dedicated, queue-based astrophysical observatory. In addition to these unique attributes of the EXI observations, the similarities with other missions allows for the leveraging of both past and concurrent observations. For example, with MARCI, one can build on the ~6 Mars years of daily global UV images as well as those taken concurrently with EXI.

The Emirates Mars Mission
Edited by Dave Brain and Sarah Yousef Al Amiri

Extended author information available on the last page of the article

Table 1 EMM Science Flow Down

Motivating Questions	I.	How does the Martian lower atmosphere respond globally, diurnally and seasonally to solar forcing?	II.	How do Conditions throughout the Martian atmosphere affect rates of atmospheric escape?	III.	How do key constituents in the Martian exosphere behave temporally and spatially
EMM Objective	A.	Characterize the state of the Martian lower atmosphere on global scales and its geographic, diurnal and seasonal variability. (EMM Investigation 1&2)	B.	Correlate rates of thermal and photochemical atmospheric escape with conditions in the collisional Martian Atmosphere. (EMM Investigation 1–4)	C.	Characterize the spatial structure and variability of key constituents in the Martian exosphere. (EMM Investigation 4)
EMM Investigation	1. Determine the three-dimensional thermal state of the lower atmosphere and its diurnal variability on sub-seasonal timescales.		2. Determine the geographic and diurnal distribution of key constituents in the lower atmosphere on sub-seasonal timescales.		3. Determine the abundance and spatial variability of key neutral species in the thermosphere on the sub-seasonal timescales.	4. Determine the three-dimensional structure and variability of key species in the exosphere and their variability on the sub-seasonal timescales.
Instruments	EMIRS		EMIS, EXI		EMUS	EMUS

1 Science Background and Rationale

EXI's capabilities and performance requirements are driven by its role as an atmospheric experiment, and in particular by the inputs that it can provide to the overall EMM science investigation. As discussed by Amiri et al. (2021), the EMM objectives and associated investigations flow down from basic, big-picture questions. EMM leverages the synergy between three science instruments to characterize aspects of global circulation and to probe the connections between the lower and upper atmosphere; in alignment with MEPAG Goal II (MEPAG 2020). In addition to the complementary nature of the instruments, EMM contemporaneously samples both diurnal and seasonal timescales on a global scale. The general details of the flow down are given in Table 1, where it is seen that EXI specifically contributes to Investigation 2. More specifically, EXI measures the spatial and temporal distribution of key constituents. In addition, though not indicated in the table, EXI also provides inputs to Investigation 1 through albedo boundary condition of atmospheric energy balance.

The specific studies planned with the EXI data include (1) the distribution of aerosols and ozone column-integrated values in the Martian atmosphere, (2) the detection and the tracking of dust storms from the local scale (*i.e.,* tens-to-hundreds of km) to the planet-encircling events which occur every few Mars years, and (3) the determination of absolute reflectance values of the surface in the visible and the characterization of seasonal changes at the scale of several km. These areas of investigation are discussed briefly below.

1.1 Clouds

Water ice clouds play an important role in the Martian atmosphere. Their microphysical and radiative properties can have a large effect on atmospheric radiative balance while their formation processes can perturb both small and large scale atmospheric circulation patterns (*for*

example., Clancy et al. 2017, and references within). Detailed understanding of the interactions of clouds with the atmospheric system typically involves comparing observations to the atmospheric state predicted by dynamical models. Consequently, the quantitative characterization of their horizontal and vertical distributions represents an important part of constraining and improving such models (and their associated physics). Naturally, global synoptic observations would constitute a fundamental dataset and progress in this direction has been made in the last 15 years through data obtained by MRO. In particular, the Mars Climate Sounder (MCS; McCleese et al. 2007) and MARCI (Malin et al. 2008) provide systematic spatial coverage of the vertical and horizontal extent of water ice clouds. However, things are quite limited from the perspective of diurnal coverage, due to the Sun-synchronous orbit of MRO. The amplitude of the diurnal variations of water ice cloud abundances can be seen clearly in previous EXI-like views of the aphelion cloud belt obtained by the Hubble Space Telescope images over 20 years ago (*i.e.,* James et al. 1996; Wolff et al. 1999).

Unfortunately, EXI will not be able to distinguish between water ice and CO_2 ice. However, the latter types of clouds will contribute very little opacity to the column-integrated optical depth retrievals to be formed, particularly when considering the 2-4 km footprint (at nadir) of a single pixel and the need for solar illumination, *i.e.*, no polar night observations (Clancy et al. 2007, 2017).

1.2 Ozone

The presence of ozone in the Martian atmosphere was recognized early in the era of spacecraft studies (cf. Barth et al. 1973). Its interaction with the Martian atmosphere is similar to that for the Earth, *i.e.*, it is anti-correlated with water vapor. It is this aspect of ozone that has typically motivated much of the recent interest in Martian ozone; namely that presence of ozone serves as a proxy for water (or rather the lack thereof) (cf. Clancy et al. 2016, and references contained within). However, when one considers the use of images to measure ozone, one can also take advantage of ozone as a tracer of dynamical activity (*i.e.,* weather systems) when the water vapor abundance varies spatially as the phenomena propagate; as was demonstrated by the MARCI instrument (Clancy et al. 2016). As with clouds, measuring the abundance as a function of location, season, and time-of-day can provide very useful insights into the behavior of the lower atmosphere. With EXI (*i.e.,* diurnal and near-global spatial coverage), constraints could include an additional probe of the amount of water vapor and a characterization of transport processes through the tracking ozone features associated with weather phenomena.

1.3 Dust Storms

Martian dust is a fundamental driver of atmospheric weather and climate. For example, it serves as the primary energy source of atmospheric motions through the absorption of solar radiation and provides non-linear interactions with the water cycle through the nucleation of water ice clouds (*i.e.*, Kahre et al. 2017, and references within). As with other atmospheric constituents, knowledge of the dust distribution is an important part of characterizing the lower atmosphere. However, much of the atmospheric dust comes from lifting events known as "dust storms". Significant progress has occurred over the last 15 years in quantifying the growth and evolution of dust storms through the global imaging provided by Mars Observer Camera (MOC) and by MARCI (*e.g.* Cantor et al. 2010). EXI can play a principle role in further investigations by providing spatial coverage on timescales less than the 1 Martian day sampled by MOC and MARCI. In addition, the continuing operation of MARCI offers the opportunity of additional time resolution from the combined datasets.

1.4 Thermal Inertia

The surface of Mars plays a fundamental role in the energy budget of the lower atmosphere. That is to say, in order to understand the contribution of the surface, one must understand the relevant radiative properties of the surface. And analogously to the atmospheric constituents, one must determine these surface properties as a function of location (and to a lesser degree of time). One such surface property is that of thermal inertial (TI), which represents the ability of a material to absorb solar energy during the day, conduct it into the subsurface, and then re-emit that energy during the night (Kieffer et al. 1973). Because thermal inertia is connected to the underlying geology (*e.g.*, composition, structure, etc.), spatial variations are due to changes in the geology. While global datasets of TI have been tabulated from the Viking and MGS missions, issues remain due in part to the very limited diurnal coverage (Christensen 1982; Jakosky et al. 2000). Consequently, an improvement in understanding the TI — and thus to knowledge of the lower atmosphere — can be made by combining the measurements of two EMM instruments: EXI for surface albedo and EMIRS for surface temperature. Lambert albedo will be calculated using the calibrated radiance from the visible f635 channel. We will compare our results to Thermal EmissionE Spectrometer (TES) albedo data acquired during similar Ls and observation conditions. Similar to methods and results described in (Edwards et al. 2011), we anticipate applying an offset to the EXI albedo, which is due to the nature of the two instruments; TES albedo values are derived from broadband (0.4–2.7 μm) whereas EXI albedo will be derived from a single band (635 nm) that only spans a fraction of the spectrum. In addition, together they will provide a robust estimate of the atmospheric state, which is necessary in removing the effects of the atmosphere from the measurements of the albedo and temperature.

1.5 Limb Observations

Observations of the Martian limb will be present in almost every EXI image of Mars, allowing one to probe systematically the vertical structure of the atmosphere. By combining the UV and VIS bands, one can derive vertical profiles of aerosols and ozone with a resolution of 2–4 km and at a variety of local times. However, the spatial coverage will be quite limited; and when considering the added complexity associated with multiple scattering radiative transfer-based limb retrievals, the decision was made to exclude such analyses from the baseline science goals. Nevertheless, such retrievals could be made by interested members of the science community once the data products are publicly available

2 Instrument Implementation

To fulfill the science objectives outlined above the Emirates Exploration Imager (EXI) was developed as a six-band ultraviolet-visible (UV-VIS) spectral imager to provide high fidelity full-disk images of the planet from the Emirates Mars Mission (EMM) spacecraft orbit in the UV and VIS spectral bands listed in Table 3. The images have a resolution element sample grid of 10 km or less, corresponding to 46″ from orbital altitude, and a goal for each resolution element to have radiometric uncertainty less than 5% for the UV and f635 channels. EXI has an additional non-scientific requirement to take high-quality images in the visible red, blue, and green.

The EXI instrument comprises two separate units: the Sensor Head that contains all the optics and detectors, and the Electronics box (Ebox) that provides the interfaces to the spacecraft and all the electronics needed to control the instrument. The mass, power and data rates for EXI (Ebox and Sensor Head) are given in Table 2.

Fig. 1 The EMM instrument panel mounted on the Hope Probe / Al-Amal spacecraft showing science instruments EXI, EMUS, and EMIRS. The gold Multi-Layer Insulating (MLI) blankets wrap the panel and instruments to provide a stable thermal environment. The star trackers are also mounted to the instrument panel giving rigid coupling between the instruments and the guidance system to provide accurate pointing for the instruments
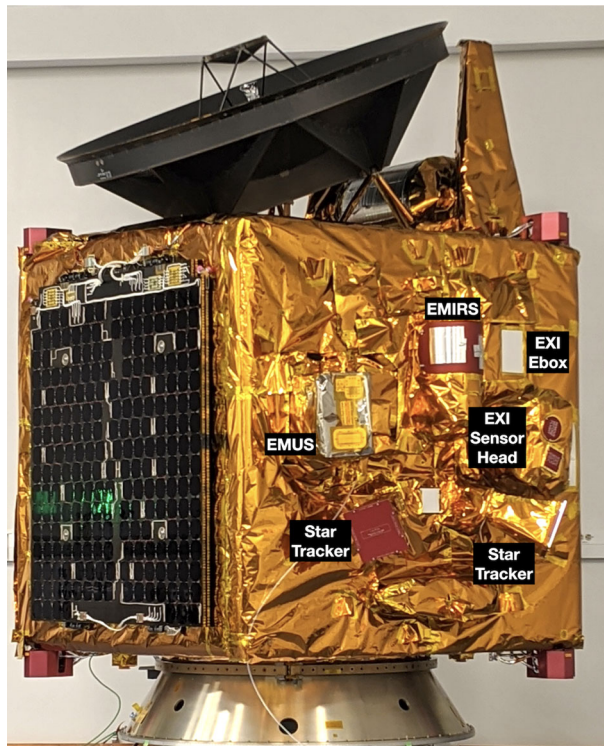
Table 2 EXI Resource Utilization. The power numbers include heater power to maintain EXI at operating temperature

Mass (kg)	Power (W)		Dimensions (cm)		Data (Mbit/week)	
	Nominal Observations	Standby	Ebox	Sensor Head	Science	Housekeeping
16.92	31.9	30.0	8.05×26.54×26.67	32.77× 36.07×39.88	3285	134

2.1 Mechanical

2.1.1 Structure

Mechanically, EXI comprises two separate units, the Ebox and the Sensor Head, shown in Fig. 1. The Ebox houses most of the electronics on the MArs diGital Image Compression (MAGIC) and PoweR sErviceS elecTrOnics (PRESTO) boards, and provides the interfaces to the spacecraft (S/C). The EXI Sensor Head houses the optical elements of EXI: detector assemblies, lens assemblies, door and filter wheel mechanisms which are all mounted to a common optical bench (the Lower Interface Plate (LIP) in Fig. 2). The LIP is then mounted to the primary structure of EXI Sensor Head (Fig. 2). The baffles and detector radiators are separately mounted to the Sensor Head structure, and the entire system is built to be light-tight when the door is closed.

The UV and VIS lens assemblies, though separate, use exactly the same construction and alignment methods. Multiple individual lens elements were purchased and the focal length
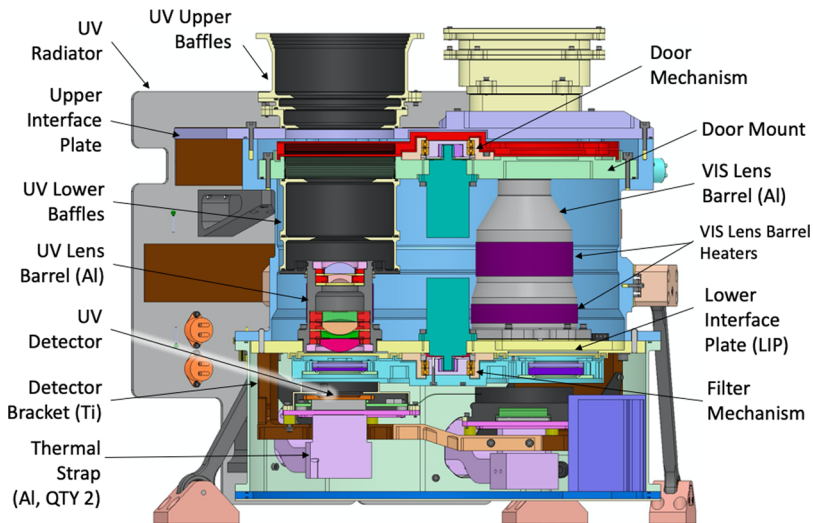
Fig. 2 EXI Sensor Head overview (UV Channel in cross-section)

of each lens element measured individually. A ZEMAX optical model using these measured properties was used to create the best-performing element sets. Each optic is individually aligned and bonded into a circular mount and then stacked into a barrel using shims to control the spacing between each lens to <13 μm. The fit between the outer diameter of the optic mounts and the inner diameter of the lens barrels is a tight fit to maintain concentricity of the system. After the lenses have been shimmed and stacked into the lens barrel they are clamped into place with a custom retainer nut that preloads mounts to the lens barrel. This approach was used previously on the Cloud Imaging and Particle Size Experiment (CIPS) camera built by LASP (McClintock et al. 2009) aboard the Aeronomy of Ice in the Mesosphere (AIM) spacecraft. Alignment of the individual lenses into their mounts utilized the TriOptics OptiCentric 100 autocollimator. Typically the optical axis of the lenses were aligned to within 5 μm of the mount ring center. Once the lenses were aligned they were bonded to the mount ring with Hysol 9309 injected onto 4 bond pads evenly spaced around the lens. Bond lines were controlled to be between 125 μm and 635 μm in thickness. The outer surface of the lens barrels have Kapton film heaters installed, which are used to maintain the optics at +21 °C to avoid thermally induced misalignment.

The detectors are held rigidly in place with titanium (Ti-6Al-4V) brackets to provide thermal isolation from the rest of the structure. During assembly the detectors are shimmed for center and focus. A flexible aluminum foil thermal strap is used to connect each detector to its radiator. All bolted joints in the thermal path from detector to radiator use indium foil for improved thermal conductivity. On the back of each radiator is also a heater patch and thermistor that are used to maintain the detectors at the operational temperature. The back of each radiator also has a second heater patch and mechanical thermostat that provide survival heat when EXI is not powered.

The Sensor Head is mounted to the spacecraft using three pairs of bi-pod kinematic struts using a design similar to that flown on previous instruments. This provides a perfectly constrained, and not over-constrained means of repeatably mounting the EXI Sensor Head with no thermal stress. This system also provides both high mechanical damping, and thermal isolation.

To keep the optical system as clean as possible the Sensor Head has active purge for all ground operations. The Sensor Head can be considered to have three zones. At the bottom are the detectors which have the most stringent cleanliness requirements, so the GN_2 starts in the detector zone, it then flows up past the filters through the lens assemblies, through the door and out of the instrument through the baffles. The detector and associated power electronics are located together on a rigid-flex circuit board referred to as a "Bunny Board" (see Fig. 6). The Detector is on a separate end of the rigid-flex and is isolated from the rest of the electronics, which are in their own enclosure, to mitigate the source of contamination. The electronics have their own vent path out of the instrument separate from the purge vent path. The vent utilizes a torturous path to maintain light tightness. These are the same paths by which air escapes from the instrument during launch.

2.1.2 Mechanisms

The EXI has two, almost identical mechanisms, a door mechanism and a filter wheel. These are based on LASP heritage designs from previous flight instruments scaled to EXI's requirements. They both use the same Avior 3-Phase DC stepper motors, with a natural step size of 30° with a right angle gearbox with a 72:1 gear ratio that provides a nominal step size of ∼0.42°. Position feedback comes from a resolver built into the actuator assembly that has an accuracy of 0.13°. By using such a design that works for both the door and filter-wheel mechanisms life testing was simplified, *i.e.,* requiring life testing on only a single motor/gearbox assembly to qualify it for both applications.

The door wheel has two openings 135° apart, both wide enough to allow light to enter either the UV or VIS lens system unobstructed. This arrangement provides the flexibility to expose the UV and VIS lenses individually, or together. The rest of the wheel is solid metal and closes the entry to the lenses, providing optical and contamination protection. Most of the time the door closes both channels, and is only opened just before measurements are to be made, keeping the optics as safe as possible. The door was used to expose only the individual channels to check that there was no measurable crosstalk between the UV and VIS optical channels. The door was used to reduce contamination of the EXI optics when on the ground, and is used to prevent accidental solar exposure on-orbit. To this end, only very specific operational modes allow the door to be opened, if a command is sent to open the door when not in the correct mode the command will be rejected (see Fig. 8)

The filter wheel has six openings that hold the band-limiting channel filters. Though all the filters are on the same axis, the UV and VIS filters cannot be used interchangeably between channels (though light will pass through them) as the UV and VIS lenses and filters are optimized for their own channel. The filters are arranged 45° apart on the wheel, so that a UV and VIS exposure can be made without moving the filter wheel. This arrangement also provides a blank position that stops light from the lenses reaching the detectors. This is used when stimulus lamp images (used to periodically check for changes in pixel-to-pixel variation) are taken and is considered as the safe (Sect. 2.7) position for the filter-wheel, by providing the most protection to the detectors.

These mechanisms are vital to the correct functioning of EXI, with the door providing the major component in the protection of EXI. Consequently, the mechanisms were extensively tested. As well as the mechanism life testing already mentioned, they were subjected to vibration testing early in the program and were also tested at the lowest and highest voltages expected and at hot and cold temperatures to verify their performance.

Fig. 3 Optical Layout of EXI
showing the baffles, door
mechanism, lens assemblies
made up of the lens tubes with
lens elements, filter wheel, and
detectors
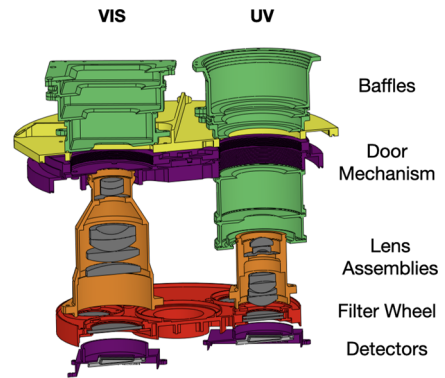
2.1.3 Mechanical Interfaces to the Spacecraft

Both the Ebox and the Sensor Head are bolted to the spacecraft using thermally isolating joints. While the Ebox is directly bolted down, the Sensor Head uses pinned joints and kinematic struts to hold tighter tolerances on the pointing. During the development of EXI and the spacecraft interface, it was determined that this type of interface was sufficient to define the instrument pointing well enough that shims are not required. This has been borne out in the initial stellar observations by EXI showing that the EXI boresight to spacecraft alignment is within $20'$.

2.2 Optics

To cover the broad spectral range, the UV and VIS are separated into two channels having different optical paths and detectors (Fig. 3). The general specifications for each are listed in Table 3. The UV lens is optimized for the three bandpasses in the range of 205–335 nm using six elements comprised of fused silica, CaF_2, and MgF_2. Due to design challenges associated with correcting the lens in the spectral range, optimization was limited to the circular science field-of-view (FOV) of the Mars disk, rather than the full detector frame. The VIS lens is designed with a similar FOV and resolution as the UV channel, but having an f/# to accommodate the brighter visible spectral region. It consists of four elements of radiation-hardened glasses from Schott and Sumita; two of the elements are cemented doublets. The optical boresights of the UV and VIS channels are coaligned to $< 40''$.

Both the UV and VIS lenses are designed to be telecentric in image space so as to have a constant incident angle on the filter for all field angles to avoid detuning of the filter across the field of view (Fig. 4). The UV and VIS channels share a common filter wheel that places a one or two element thin film bandpass filter between the lens and detector of each channel. The thickness of the filter is used to correct the focus for each channel. Each lens has a front baffle to suppress glare from sunlight or glints from nearby spacecraft components. In addition, the UV and VIS lens elements each have optimized anti-reflection coatings to reduce internal, in-band, scattered light and glare at the detector.

The ZEMAX Optic Studio software was used to optimize the lens designs and ensure that mechanical tolerances would be sufficient to assemble lenses that met requirements, while the FRED Optical Engineering software was used to model the scattered light properties of the design.

Fig. 4 ZEMAX raytraces of the EXI UV and VIS optical systems (the relative scale between the channels is correct)
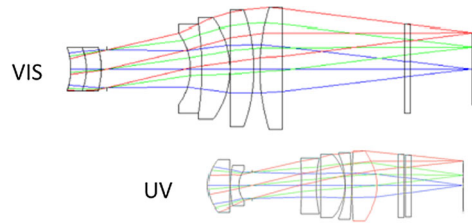
Table 3 EXI Optical Design Prescription

	UV Channel	VIS Channel
Focal Plane Format	12.6 MP 4:3 format	
	4096×3072 @ 5.5 μm	
Technology	CMOS	
Dynamic Range	12-bit, 13,500 electrons full well	
Focal length	47.5 mm	50.6 mm
Effective Area	128.89 ± 0.23 mm^2	112.651 ± 0.087 mm^2
f#	3.7	4.2
Field-of-View	18.6°	25.8 × 19.3°
Pixel Angular View (on axis)	$< 23.9''$ per pixel	$< 22.4''$ per pixel
Filter Spectral Bands	f220: 205–235 nm	f437: 427–447 nm
	f260: 245–275 nm	f546: 536–556 nm
	f320: 305–335 nm	f635: 625–645 nm

2.3 Detector

Data from both the Centre National d'Études Spatiales (CNES) (personal communication (A. BenMoussa) and Adamiec et al. 2019) and the Solar Orbiter Extreme Ultraviolet Imager (EUI) development (BenMoussa et al. 2013a) suggested that the CMOSIS CMV process was suitable for space instruments. The CMV 12000 (4096×3072 pixel) sensor had a form factor, pixel count, and availability that made it the only viable single sensor option at the time of the EXI initial instrument design. The sensor was bought as a commercial device but specified without micro-lenses, monochrome (no Bayer filters) and with a removable window. A flight lot of 10 packaged devices (and additional unpackaged die) was procured so that a limited lot acceptance protocol could be applied, involving burn in (all devices), radiation testing (1 device), accelerated life testing (1 device), and wire-bond pull, die-attach, and Destructive Physical Analysis (DPA) (1 device). This left enough devices for flight and flight spares. These remaining devices were further tested for QE, noise, and dead/hot pixels and ranked for suitability in the UV or VIS channel.

The linear range of the DN vs. incident intensity was measured in the laboratory by using a stable source of illumination and taking images with different exposure times. The detectors were measured to be linear to >95% full well (Fig. 5). The exposure calculations are based on a full well of 75% Any non-linearity will be corrected on a per-pixel basis in ground processing if necessary.

Both detectors are maintained at ~-10 °C during nominal operations to keep both the intrinsic, and radiation-induced dark current low.
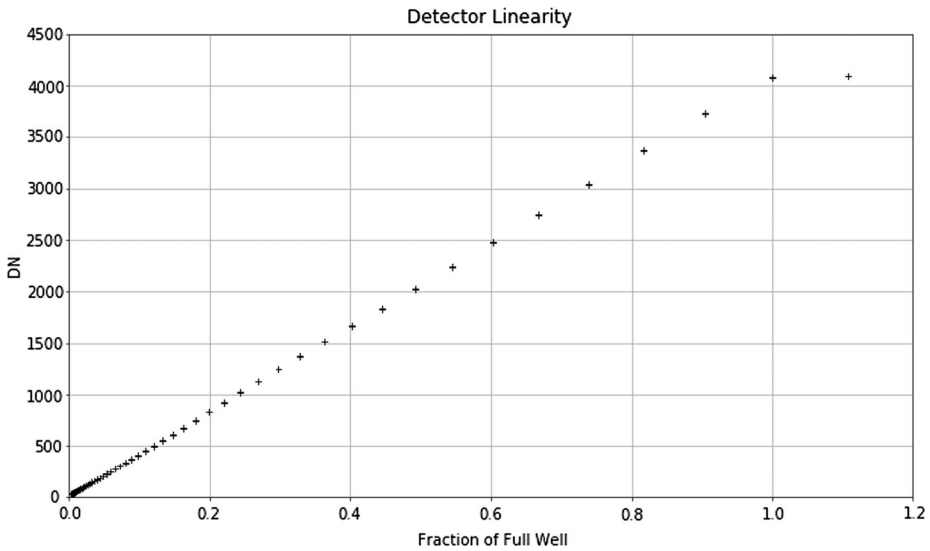
Fig. 5 EXI Detector SN4 linearity measurements show the very linear behavior of the CMV 12000 detectors. The detectors have on-chip digitization of the pixel signal, black-Sun correction and correlated double sampling (CDS)

2.3.1 Radiation Testing

The architecture of the CMOSIS CMV-detectors has a known non-destructive Single Event Latch (SEL) behavior (identified in radiation testing by Centre National d'Études Spatiales CNES) characterized by a higher current operating mode in the device that does not affect performance, and possible Single Event Functional Interrupt (SEFI) (BenMoussa et al. 2013a). To characterize these behaviors Single Event Effects (SEE) testing of one of the flight batch of detectors was performed at the Texas A&M Radiation Effects Facility. The EXI team worked with Radiation Test Solutions to obtain beam time and develop a testing plan to fully characterize the detector. While testing the Single Event Upsets (SEUs), non-destructive SELs and SEFIs were observed. The SEFI manifests by the detector becoming totally uncommunicative, and requiring a full power cycle to return it to its nominal operations. All these SEEs have been accommodated in the defined detector operations. While exposing the test device to heavy ions Total Ionizing Dose (TID) was accumulated in the silicon. During the testing the detector showed some increase in dark current with dose. However, as the test was not designed to characterize TID we do not have the data to characterize dose related effects. The key results are:

- No destructive SEE effects to the highest level tested, 42 MeV cm^2/mg (requirement: no destructive SEL at <37 MeV cm^2/mg)
- High current SEE modes exist that are not related to register upsets, and require power cycling for recovery. These events did not impact the functionality of the device other than the increased current draw. These high current modes should be considered as a SEL
- SEFI, register SEU, pixel SEU, and stuck pixel (i.e. "hot pixel") SEU modes were observed
- Two irradiation zones were used, and there was an overlap between the zones. Zone 1 did not include the registers and Zone 2 included the registers. The TID exposures are as follows:

- – Zone 1: 2.9 krad (Si)
- – Zone 2: 10.4 krad (Si)
- – Overlapping region: 13.3 krad (Si)
- Testing verified that the EXI flight software over-current detection and correction algorithms captured high current events and restored functionality

2.3.2 Detector Operations

At power-on, the CMV 12000 enables all 64 Low Voltage Differential Signal (LVDS) outputs. EXI only uses two of the outputs, so the first action is to set the device to output on just 2 LVDS channels. This drops the power consumption of the detector by 2.5 W. During the instrument thermal-vacuum testing the measured "warm-up" time from power-on to a stable temperature was about 50 minutes. So before any science measurements are made the detectors are configured for nominal operating conditions at least 50 minutes before the measurement. If a second set of measurements are required by the Concept of Operations (ConOps, see Sect. 4) — for instance the X-OS2 observation following an X-OS1 observation within 50 minutes the detectors will be left on.

To accommodate SEUs in the control registers (that define the operation of the detector), all 128 registers will be written immediately before each image capture, and then all 128 registers will be read back immediately after the image capture and compared with the expected values to determine if any upsets occurred during the image capture (it requires less than 10 ms to read/write all registers). Any register discrepancies are reported with the image data.

Similar to the detection of the non-destructive SEL and SEFI noted above the currents of both detectors are constantly monitored. If the current rises above a threshold value the power to the detector is recycled, and a counter is incremented to flag that this happened. Should the power cycle not reset the SEFI, power is removed from the detector and an error flag raised by the EXI flight software so that further investigation can be carried out by engineers on the ground.

2.4 Cleanliness

Experience has shown that organic and particulate contamination of optical surfaces leads to degradation of optics in space (*for example,* BenMoussa et al. 2013b). To keep EXI as clean as possible, and so reduce the on-orbit degradation, the instrument was fabricated and tested in clean rooms with humidity, particulate, and volatile chemical controls. Materials were carefully chosen (for both flight and on-ground support equipment) not to introduce contaminants, and all flight materials are vacuum backed, again in an effort to minimizes contamination of the instrument. On the ground, special covers were fabricated that covered the baffles and added an extra layer of protection. For transport, environmental testing and storage EXI was kept in a clean, purged bag that was only removed in a clean environment.

There are obviously times when an instrument cannot be in a clean room, for example some testing environments, shipping and launch operations. For as much of the time as possible when the instrument is not in a clean environment, it is kept with aperture covers and bagging to protect the optics, and under active GN_2 purge. Experience has shown that the cleanest way to purge an instrument is to use the gas boil-off from LN_2 that is then flowed through a clean molecular sieve canister before reaching the instrument. The clean gas is distributed using a low-pressure regulator and Mott filter to the instrument optical cavities, with care taken to ensure that the vent paths are from the most sensitive optical
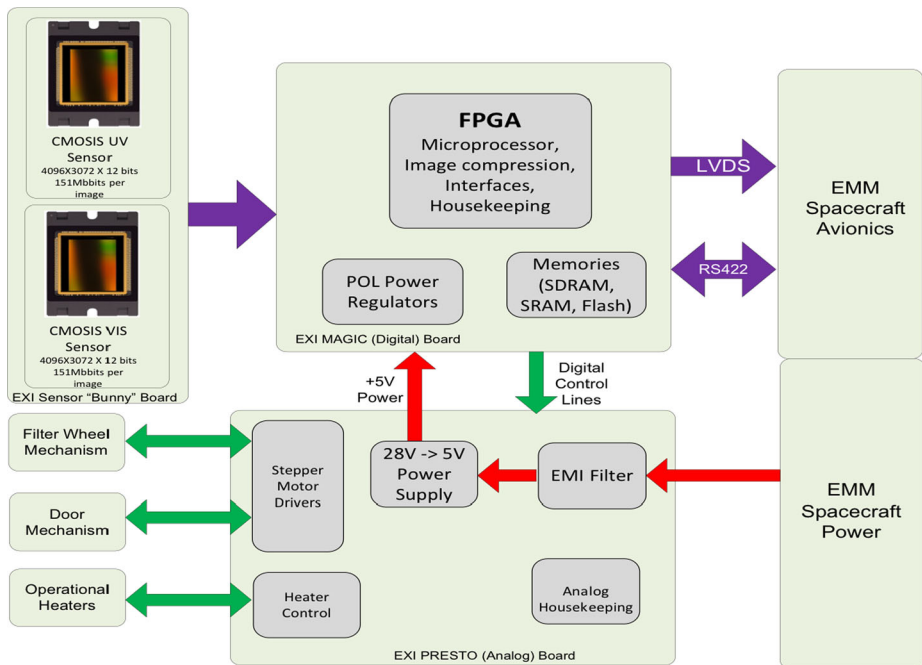
Fig. 6 A block diagram of the EXI electronics and their interconnections

components to least sensitive mechanical structures. This vent path design also takes into account the optimum ways to maintain cleanliness during depressurization of the instrument during both on-ground testing, and the ascent to orbit. These are all captured in an Instrument Contamination Control Plan (CCP), which feeds into the overarching Spacecraft CCP.

2.5 Electronics

The electrical subsystem of EXI could be considered the brains and circulatory system of the instrument. It consists of analog and digital functions that are mostly segregated on separate boards. A simplified block diagram is shown in Fig. 6

2.5.1 Analog Electronics

The power and analog electronics are located on the PRESTO board in the Ebox. PRESTO distributes the power coming from the S/C, limits the inrush current, and multiplexes the housekeeping signals. A DC-DC voltage-converter provides isolated, regulated 5.0 V to the MAGIC and BUNNY boards. PRESTO also provides power for the door and filter wheel, power conditioning for the detector and lens heaters, and provides multiplexing for all the housekeeping signals that monitor temperatures, voltages, and currents included in the instrument telemetry.

   To minimize noise and to provide better signal integrity, the voltage regulators for the detectors are placed on separate BUNNY boards close to the detectors in the Sensor Head. Separate Low Drop Out (LDO) regulators are used for each detector to create the 3.3, 3.0, and 1.98 V supplies needed for each detector. The supply current to each detector is monitored on the MAGIC board and if a higher current than expected is encountered (due to

Table 4 EXI FPGA functionality

Microprocessor	32 bit Microblaze processor (Flight Software)	
	NOR flash controller	
	SRAM interface (Image storage)	
	SPI interface (Detector control)	
Detector Interface	Image integration timing	
	Dynamic IO skew correction	
	Training pattern recognition	
	147 MHz detector interface clock	
	73 MHz DDR LVDS serial data	
	Data DMA to SDRAM pixel buffer	
Image Processing	Region of Interest (ROI) calculations	
	Pixel Thresholding	
	Image histogram calculation	
	Image pixel binning 1×1 to 32×32	
	JPEG-LS lossless compression	
Spacecraft Interface	5 MHz LVDS link to S/C for science data	
	115 kbaud RS422 link to S/C for housekeeping and commanding	
	Create CCSDS data packets	
	Receive CCSDS commands from S/C	

the SEL/SEFI effect in the detector (Sect. 2.3.1)) the LDOs for that detector will be power cycled to clear the SEL/SEFI. The detectors, and their power supplies mentioned above, together with the lens and detector heaters, are the only active electronics in the Sensor Head.

The MAGIC board also has individual point-of-load regulators for the Field Programmable Gate Array (FPGA) and its associated peripherals that draw their power from the PRESTO board.

2.5.2 Digital Electronics

The control of EXI is built around a Xilinx Virtex 5QV re-programmable FPGA. This controls the entire instrument either directly through the FPGA logic, or via an embedded MicroBlaze microcontroller that runs the EXI Flight Software (FSW).

The FPGA and most of the support interfaces are located on the MAGIC board in the EXI Ebox. The FPGA is the heart of the EXI operations, providing all functionality (Table 4) needed to acquire, process, and transmit the images, receive commands from the spacecraft, as well as all the other functions needed to keep the instrument operating safely.

As the radiation environment can cause upsets in the various memories accessed by the FPGA, mitigation strategies are employed to ensure that the contents of memory are preserved intact. Specifically, Error Detection And Correction (EDAC) is used on all block RAMs in EXI, tabulating the number of corrections made and reporting these values in the housekeeping data. Additionally, the FPGA is periodically (every month) power cycled as a best-practice activity in order to reset any accumulated SEUs.

Camera Control

The FPGA receives image data from the CMV 12000 sensors via two Double Data Rate (DDR) LVDS lines at 147 Mbit/s (294 Mbit/s total data rate). A training pattern generated by the sensor is used to establish bit-lock on the LVDS signal. EXI uses the Xilinx programmable input-output (IO) delay to automatically optimize the interface timing for maximum setup and hold time. As the data are received the FPGA packs two 12 bit pixel samples plus 8 bits of Error Correction and Detection (EDAC) into each 32 bit word and writes data to Synchronous Dynamic Random Access Memory (SDRAM).

The FPGA can be commanded to provide two different deterministic test patterns that can be used to verify end-to-end system integrity. Either a pattern generated by the FPGA or one built into the detector can be used depending on the state of the instrument. These patterns are useful for verifying bit-accurate transmission of data both in the instrument and through the entire chain from the instrument to the ground, and subsequently through the data processing system.

Compression Core

To reduce the data downlink all the images are compressed with JPEG-LS (Weinberger et al. 2000). The compression is performed in the FPGA using an Intellectual Property core (IP core) developed and tested at LASP. The JPEG-LS standard (ISO-14495-1/-ITU-T.87) specifies both lossless and lossy modes, the core developed for EXI implements both options, but only the lossless mode has been rigorously tested. JPEG-LS was used by Jet Propulsion Laboratory (JPL) on the Mars Exploration Rovers.

Data Handing

There are several onboard data handling options that can be applied to the data in order to reduce the data volume sent to the ground. All options can be commanded by EXI FSW, and are implemented in the FPGA.

Binning: Though there are operating modes in the detector that allow binning pixels together, we chose to implement this functionality in the FPGA, as the on-chip version limits the binned pixel to only the full-well of a single pixel. EXI FSW can request data binning modes from no binning to 32×32 pixel binning — giving the smallest image size of 128×96 pixels.

ROI: Since most of the science campaign observations target only the disk of the planet, we have implemented a number of circular "regions of interest" (ROIs) that can be used to isolate the planetary disk (without encroaching on the limb) so that off-disk data is set to zero.

Compression: As noted above, JPEG-LS has been implemented as an IP core in the FPGA. Although it is intended that only the lossless compression mode will be used by EXI, the lossy compression is also implemented in the IP core.

Any combination of the data modification schemes can be applied to each image as it is processed by the FPGA but compression, if applied, must be the final step.

Processed data from the detectors can be stored locally in the EXI Static Random Access Memory (SRAM), or transferred to the spacecraft where it is stored for later transmission to the ground.

Reprogamability

While the Xilinx Virtex 5QV is a fully reprogrammable FPGA, it is "brain dead" at power on, and must load a bitfile from an external memory. EXI uses a one-time programmable

Programmable Read Only Memory (PROM) to store the EXI default FPGA configuration. NOR Flash is used to store up to two modified images, and can be updated in flight. A Boot Select signal from the S/C will select whether to boot from PROM or flash. The FPGA will automatically fall back to the PROM if it fails to boot from flash. EXI FSW scrubs the NOR flash to prevent the build-up of SEU errors.

2.5.3 Electrical Interfaces to the Spacecraft

All the electrical interfaces between EXI and the spacecraft are connected through the EXI Ebox. The PRESTO board is the power interface, while the MAGIC board handles the data interfaces (see Fig. 6). The bidirectional low-rate data for commanding EXI and for the housekeeping data returned from EXI using a 1553 Space Wire protocol. Additional electrical signals include a time signal from the spacecraft that is used to synchronize the EXI clock, the current vector to the Sun, andto provide a watchdog confirming that the spacecraft can communicate to EXI. These signals are provided over an RS-422 interface. EXI uses the S/C provided Sun vector to determine when the Sun encroaches into EXI's 'Sun keep-out zone'. If the Sun keep-out zone is encroached, or communication is lost with the S/C, EXI will autonomously close the door if it is open. A separate line is provided to let the spacecraft control which boot image for the FPGA is to be used. The high-rate science data interface is an LVDS interface to the S/C.

2.6 Thermal

EXI does not have very stringent temperature requirements, but in order to meet its performance requirements, the lenses and the detectors do need to be kept at stable temperatures. This is achieved by using passive radiators looking at deep space, and active heaters to bring the components to temperature.

The Operational Heaters are located on the detector radiators (Sect. 2.1) and lens assemblies. There are 4 circuits: 2 radiators and 2 lens assemblies. The heaters are single string with redundant control sensors that are controlled by the flight software. Switching to the redundant control sensor is not automated and requires ground intervention. Heater setpoints can be adjusted in flight but the detectors are nominally kept at $-10\,°C$ and the lenses at $+20\,°C$. Stability is maintained within $\pm1\,°C$ of the setpoint while operating.

To maintain the FPGA in the Ebox at a safe temperature there is a radiator on the top cover of the Ebox which is connected to a thermal spreader integral to the Ebox that provides a conductive path from the FPGA to the radiator.

Both the Ebox and the Sensor Head are also isolated from the spacecraft and the external environment by Multi-Layer Insulating (MLI) blankets that cover the entire instrument except for the three radiators and the optical apertures.

There are survival heaters on the Ebox, Sensor Head, and on each of the detector radiators. These are powered directly from the spacecraft through mechanical thermostats that are mounted on the detector radiators, Ebox, and Sensor Head. These keep the instrument at a safe temperature while the instrument is un-powered. The thermostats are set at temperatures that are lower than the operational temperatures so that they do not have an effect on the normal powered operation of EXI.

The thermal performance of the instrument was modeled, and the model verified during the instrument level thermal balance tests. Thermal performance requirements were all tested and verified during both instrument and spacecraft thermal vacuum testing.

When EXI is not powered it does not provide housekeeping data to check the instrument temperature or any way to use the instrument heaters. Therefore, the spacecraft provides
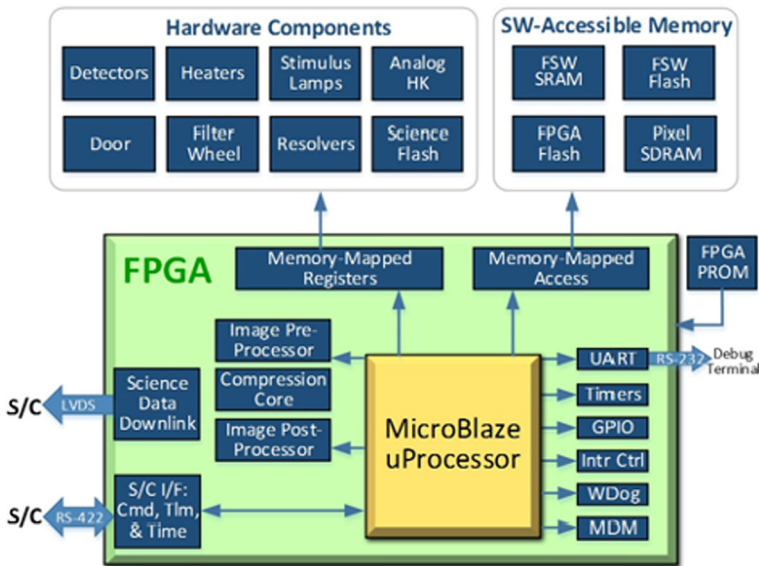
Fig. 7 EXI Flight Software environment and interfaces

temperature monitors and power for survival heaters that allow temperature monitoring, and keep the instrument safe while the instrument is unpowered.

2.7 Flight Software

If the electronics provides the brain of the instrument the flight software gives it intelligence. Everything that EXI does is mediated by the EXI Flight Software (FSW). The FSW is a small, highly modular embedded application executing on a MicroBlaze processor which is embedded in a re-programmable Xilinx Virtex5QV FPGA. The EXI FSW is composed of two single-threaded bare-metal applications that use a deterministic executive scheduler instead of an operating system. The FSW code is written in object-oriented C++ and developed using a Test Driven Development (TDD) methodology.

The FSW is responsible for operating the instrument, and primarily directing the acquisition, storage, and transmission of science images. It handles communication with the EMM spacecraft using RS-422 where it receives real-time commands and produces synchronous and asynchronous telemetry. Three on-board command sequence engines are used for science operations, mode transitions, and fault protection. FSW accesses five different types of memory, including devices used to store the FPGA and FSW images so they can be patched or modified throughout the mission. Internally stored tables and sequences are used to change FSW behavior and instrument configuration to provide flexibility during all mission phases.

The FSW never interacts directly with external hardware components — instead the FSW uses registers to direct the FPGA on how to operate hardware components. The FSW environment and interfaces are shown in Fig. 7, using colors to denote the FPGA (green box), FPGA modules (dark blue boxes within FPGA), external hardware components (dark blue boxes), and interactions with the FSW (arrows pointing away from the yellow box).

Fig. 8 EXI Flight Software Operational Modes
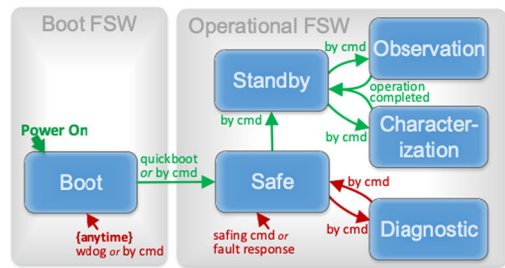
The EXI FSW is organized as seven tasks which execute at scheduled times:

Memory Task: Perform memory operations
Telemetry Task: Collects and packetizes telemetry
Command Task: Processes real-time commands from spacecraft
Command Task: Processes real-time commands from spacecraft
Upkeep Task: Perform routine maintenance and logging
Autonomy Task: Detect faults and initiate responses
Command Sequence Task: Load and execute command sequences
Science Task: Capture and process science data

EXI FSW was developed using documented engineering practices/procedures that are compliant with NASA 7150.2, which governs software engineering tasks including heritage analysis, requirements development, design, coding, developer testing, integration, and acceptance testing. Documented procedures control full traceability from requirements to design to test with rigorous and independent verification testing of both functional and performance requirements.

EXI can exist in 6 software-defined modes that define which commands are acceptable, and what actions can be accomplished by EXI (Fig. 8).

Boot Mode: Intended to be small, simple, and transient at power on. It protects the detector and optics from degradation. It offers only a small subset of the Operational FSW with limited functionality, having a reduced command set focusing on instrument safety and memory operations. It is able to control the instrument heaters, and close the door, and set the filter wheel to the blank position.
Safe Mode: Keeps EXI in a safe (powered) configuration until given all-clear. The door is closed and the filter wheel in the blank position. Active thermal control of the instrument is maintained, but the detectors are unpowered. In Safe Mode, all commands that violate the safe configuration are rejected.
Diagnostic Mode: Is used to diagnose problems. It allows more freedom with motor movements than Safe Mode. EXI will always exit Diagnostic mode into Safe Mode so that results of the diagnostic data can be fully analyzed.
Standby Mode: Idle and waiting for Observation or Characterization command. EXI is almost always in Standby Mode.
Observation Mode: Perform science observations.
Characterization Mode: Perform calibrations to track sensitivity and degradation.

2.8 Science, Auxiliary Data, and Housekeeping Data

The EXI instrument has two data streams, the housekeeping (HK) data that monitors the health and safety of the instrument, and the science data (SCI).

To make certain that EXI is functioning correctly both on the ground and in space various temperatures, voltages, and currents are measured and included in the low-rate telemetry using the RS-244 protocol. This low-rate data is available from EXI whenever it is powered on. These values are constantly monitored whenever there is contact with EXI, and the values are automatically compared in the ground software and alarms raised if any value is outside expected limits.

To ensure that the detector systems are functioning as expected when the high-rate science data is not available 32-bin (32 bit) histograms of the image data from both detectors are created and sent in the low-rate housekeeping data. This is used when real-time science data is not available to quickly assess the health of the detector system.

The science data comprises images from the UV and VIS detectors. The science data is only available through the high-rate telemetry link. There is a subset of data that would normally be considered as housekeeping data but are required to understand the data coming from the detectors. These 'ancillary data' are included in the science data stream, and are also included in the image FITS header of level-1 data and above so that anybody using the data can determine the conditions under which an image was acquired.

2.9 Ground System

The EXI ground system comprises command and control, and data Quick Look (QL) workstations. The same system has been used for most of the EXI instrument development and testing and is now used for controlling the instrument in space.

The command and control system is an EXI specific implementation of the Operations and Science Instrument Support-Command Control (OASIS-CC). This provides a real-time interface to the instrument whenever the instrument is on and there is a connection. All functionality of the instrument is accessible through OASIS-CC, and the interface provides a user-friendly overview of the instrument health and safety, as well as visibility of all HK telemetry points that are color-coded to represent their state (nominal, warning, error). OASIS also provides the Colorado System Test and Operations Language (CSTOL) scripting language that is used to script entire observational sequences for EXI.

While the OASIS system provides insight into the HK data stream QL is used to view the science data. Just as OASIS provides a user-friendly interface to the health and safety of the instrument, QL provides a customizable view of the science data to quickly make sure that everything is working as expected. During tests when there is no science data high-speed stream, but the detectors are on, QL can be used to visualize the detector data histograms that are in the HK telemetry stream. QL is written as a set of python programs and was developed purely for EXI.

One of the big advantages of using OASIS and QL from early in the program is the operations and science data teams gain experience using the tools,software bugs can be corrected and enhancements can be implemented and tested before operations in space commence. For ground testing, the OASIS and QL systems are connected to a spacecraft simulator that in turn connects to EXI so that the telemetry system is as close as possible to the flight configuration.

2.10 Environmental Testing

Before delivery, the EXI instrument underwent extensive testing to demonstrate that it would survive launch and would operate successfully in space.

As mentioned in some of the subsections above, individual assemblies (such as the mechanisms) were thoroughly tested prior to integration into EXI, and after EXI was delivered to

the spacecraft many of the tests were repeated in the context of the entire spacecraft system. Acoustic testing was only performed during the S/C environmental testing.

The EXI environmental test suite comprised:

Vibration Testing (VIBE)

> EXI is mounted on a vibration table that is used to shake the instrument in the X, Y, and Z axes (one-by-one) over the frequency range of 20–2000 Hz and at different amplitudes defined to bound the forces that EXI was predicted to experience at launch.

Thermal Balance (TB)

> EXI is set-up to be in as flight-like a configuration as possible. It is mounted in a vacuum chamber which has various heating and cooling plates that are used to mimic the environment that EXI will experience in space. This test is used to verify that the thermal model of EXI correctly predicts performance, and any variances are used to update the model.

Thermal Cycling (TVAC)

> Similar to the TB tests EXI is in a thermal vacuum chamber, but this time the instrument is cycled to the limits of the hot and cold operating ranges, and full instrument tests performed at both the hot and cold limits. This was performed for 8 cycles, with 3 different simulated spacecraft voltages, so confirming that EXI will operate under any of the expected mission parameters.

ElectroMagnetic Interference / ElectroMagnetic Compatibility (EMI/EMC)

> EMI/EMC testing is performed in a room shielded from external radio frequency (RF) electromagnetic waves. The testing is designed to explore two regimes: is EXI sensitive to electromagnetic radiation in frequency ranges expected at the launch site or on-orbit, and does EXI generate any frequencies that could cause problems either for EXI, other instruments, the spacecraft, or the launch vehicle, or launch range. A set of frequencies and allowed levels are provided by the EMM project, and EXI is tested to verify that those levels are met.

During the vibration testing, a problem with the lens mounting was discovered that resulted in breaking the lens bonds, and in some cases, the lenses themselves were broken. The root cause of the lens failures was determined and corrected prior to delivery of EXI This emphasizes how important the testing is, as if these problems had not been discovered in testing the instrument would probably have failed during launch.

It was also discovered that when reading the detectors EXI generates a frequency above the allowed amplitude limit for operations at the launch site. A waiver was requested, and granted, for this specific frequency and ground operations at Tanegashima were planned so that the detectors would not need to be operated when the exceedance could have caused a problem.

EXI successfully passed all environmental qualifications prior to delivery to the spacecraft.

2.11 FlatSat and Electrical Simulator

During the development of EXI, a high fidelity Engineering Model (EM) was built to provide a test-bed for construction and techniques, software development, and calibration methods. After delivery of the EXI Flight Model (FM), this EM is connected to a S/C simulator and used to test observational command sequences on the ground before they are uploaded to

the S/C and EXI. As this system is laid out on a bench (not integrated onto a spacecraft structure) it is known as a FlatSat.

If anomalies should occur on-orbit the FlatSat will be used to reproduce the errors and test solutions before any corrective actions are taken on the in-space hardware. The on-board autonomy rules have already ensured that the EXI FM is as safe as possible..

A lower fidelity EXI simulator was also developed to let the S/C team test electrical and command interfaces before the EXI FM was delivered. This electronic simulator (ESIM) is an engineering version of the MAGIC and PRESTO boards without any optics or mechanisms and is useful for testing interfaces and software that does not depend on having realistic hardware responses.

2.12 Automation and Fault Protection

During operations EMM has limited contact with ground stations so it has to rely on automation for science observations, S/C, and instrument safety. In the case of EXI stored observation sequences are initiated by the spacecraft. These sequences are planned at least two weeks in advance of the observation. Observation sequences are tested on the ground and then uploaded to EXI before they are due to be executed. Should any off-nominal conditions occur EXI is responsible for keeping itself safe. This ranges from actions such as memory scrubbing and radiation SEE effect mitigation already described, to automatically closing the door if the Sun gets close to the FOV, and taking the instrument to Safe Mode if communications are lost with the spacecraft. Some errors (such as multiple detector overcurrent events) can not be automatically recovered from so they are flagged, the instrument is either set to safe-mode or powered off, and remains in that state until engineers on the ground can diagnose the problem. Closing the door is one of the primary ways that EXI keeps itself safe, though the instrument would not be damaged by exposure to the Sun, there would almost certainly be degradation in the transmission of the lenses (BenMoussa et al. 2013b), so when EXI is not making observations the door is closed. The spacecraft sends a Sun Vector signal at a rate of 2 Hz. EXI computes the angle between the Sun and the EXI boresight, and if this is withing a predetermined response boundary EXI will automatically close the door. There are no planned activities that would put the Sun within this response boundary, but this adds an extra layer of protection should something go wrong. If for some reason the door can not be closed EXI will alert the S/C so that it knows that EXI may be vulnerable. This will also be communicated to EXI and S/C ground teams on the next communications pass, and diagnosis will be handled on the ground.

3 Instrument Performance, Characterization, and Measurement Uncertainty

Before the design of the EXI instrument was started a software model was developed to understand the various performance requirements and uncertainties. The model uses manufacturer's data and was updated with component- and system-level measurements as they became available. This model is presented in Appendix A. A multi-step instrument characterization process was followed. First, component-level measurements are made to provide data for the selection of the best components for the flight instrument and used to update the software model to guide the required system level testing. Preliminary characterization of the full instrument is made before instrument-level environmental testing (Sect. 2.10). This allows any changes in instrument performance due to environmental stresses to be assessed. Finally after completing the environmental test suite, final full-instrument characterization is performed.

3.1 EXI Measurement Equation

Instrument characterization is driven by understanding the various terms in the measurement equation that fully describes all aspects of the instrument response. The measurement uncertainties are then calculated by propagating the uncertainties associated with each term in the measurement equation.

The observed radiance(L_0) of a location (h) on the Martian surface at a wavelength (λ) is given by:

$$L_0(\lambda) = \frac{[C(\lambda, p) \times G(p) - IM(p) - D(p)]/t}{R_0 \times Deg(\lambda, T) \times r(\theta, \phi)} \tag{1}$$

where

$$R_0 = A\Omega \times \Delta\lambda_{ch} \times QT_0(\lambda) \tag{2}$$

$$= A_D \times \frac{\pi D_L^2}{4f^2} \times \Delta\lambda_{ch} \times QT_0(\lambda) \tag{3}$$

where:

L_0 is the Martian spectral radiance at wavelength (λ)
C are the measured DN from a pixel (p)
G is the pixel's gain (corrected for non-linearity)
IM represents the various stray light contributions to a pixel
D is the dark and offset counts for pixel(p)
t is the integration time
R_0 is the on-axis response of the system
r are the off-axis corrections to R_0
$A\Omega$ is the system étendue
$\Delta\lambda_{ch}$ is the spectral width of the channel
QT_0 is the on-axis system quantum throughput
D_L is the entrance pupil diameter
f is the system focal length

The corresponding uncertainty is given by:

$$\sigma_L^2 = \frac{C^2 G^2 (\sigma_C^2 + \sigma_G^2)}{(C \times G - S - D)^2}$$
$$+ \sigma_{R_0}^2 + \sigma_r^2 + \sigma_t^2 \tag{4}$$

3.2 Geometric Characterization

To map the geometric distortion of the lens systems (UV and VIS) an in-band fiber-coupled LED illuminates a 125 mm f/15 off-axis parabolic collimator. This provides a diffraction-limited point source. The EXI instrument is mounted on a four-axis manipulator (X, Y, pitch, and yaw). To maintain the entrance pupil in the same position during pitch and yaw scans the control computer calculates the required multi-axis coordinated moves. The channel FOV is scanned in this way in a 1° grid pattern and to capture the edges and vignetting
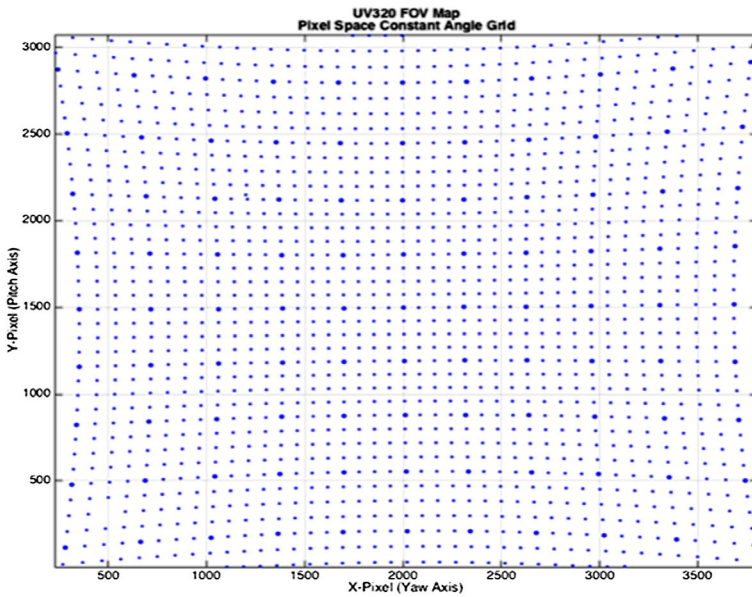
(a) UV (f320) shows mild pincushion distortion
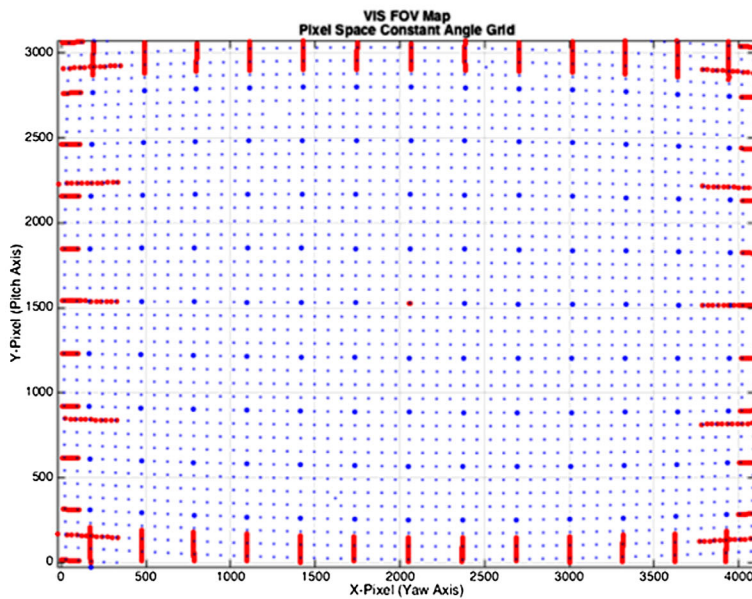
(b) VIS (f635) shows mild barrel distortion

Fig. 9 EXI Geometric Characterization Maps. Distortion corrections are applied in the Level 2 processing (Sect. 5.2)

a 0.1° grid is used along the edges of the FOV (Fig. 9). As the focus of the instrument changes slightly with ambient pressure these measurements are performed in a temperature-controlled vacuum chamber.

Table 5 EXI distortion polynomials, values are in units of pixel size (5.5 μm)

	UV			VIS		
	f220	f260	f320	f437	f546	f635
k_0 (f)	8585.485	8636.149	8733.035	9188.596	9199.021	9219.073
k_1	-2.12×10^{-8}	-3.54×10^{-8}	-2.06×10^{-8}	8.86×10^{-9}	8.78×10^{-9}	8.65×10^{-9}
k_2	-2.55×10^{-14}	-2.55×10^{-14}	-9.18×10^{-15}	-1.85×10^{-14}	0.00	0.00
k_3	9.55×10^{-21}	9.55×10^{-21}	5.18×10^{-21}	5.18×10^{-21}	0.00	0.00
RMS Error	0.883	1.336	1.219	0.607	0.640	0.896

The measured points are analyzed using the Community Sensor Model described in Sect. 3.3.3 of the Community Sensor Model Working Group (2007) This model computes distortion only, as distinct from the main term given by $r\prime = f \tan(\theta)$ in the form: $\delta r = k_1 r^3 + k_2 r^5 + k_3 r^7$ where δr is the radial distortion, and r is the radial distance from the optical center. The measured points for each filter channel were used to fit this function and the resulting corrections are used to remove the distortion in the measured images (Level 1) to produce the Level 2 products (data product levels are described in Table 9).

3.3 Radiometric Characterization

There are several steps that are required to measure the radiometric sensitivity of the EXI instrument. These include the measurements of the instrument itself, and of the transfer standard (in our case a photodiode) used to determine the source brightness.

3.3.1 Reference Detector

To tie the radiometric measurements to an absolute scale a calibrated reference detector was used to measure the irradiance of the source at the EXI entrance pupil before and after each measurement set. While the measurements were being taken relative changes of the source were monitored with a second detector so that any source changes could be tied directly to the absolute spectral power entering the instrument during the measurements.

The reference detector is a custom made and calibrated secondary radiometric standard. A micro-machined Si_3N_4 circular precision aperture (Fowler and Litorja 2003) with 19.652 mm^2 area is mounted in front of a bare 18×18 mm silicon photodiode inside a custom housing. The reference detector was calibrated in the LASP Spectral Radiometer Facility (SRF-SIRCUS) between 200 nm and 650 nm, which provides an absolute calibration tied directly to a NIST L-1 Cryogenic radiometer (traceable to the NIST Primary Optical Watt Radiometer—POWR (NIST 2020a).

3.3.2 Flat Field

Two methods were used to map the response uniformity (flat field). In the first instance a fiber-coupled laser-driven white light was used as the source for a 14.2 cm Spectralon integrating sphere with 2.5 cm exit port. A 50 cm collimating lens produced a uniform (<0.1%) radiance source that when imaged onto the detector provides a 2.4° wide "top hat" spot. Mounting EXI on a four-axis manipulator (pitch, yaw, X, Y) to maintain the entrance pupil in the same position during pitch and yaw scans using multi-axis coordinated moves,

(a) UV (F320) Flat field   (b) VIS (F635) Flat field
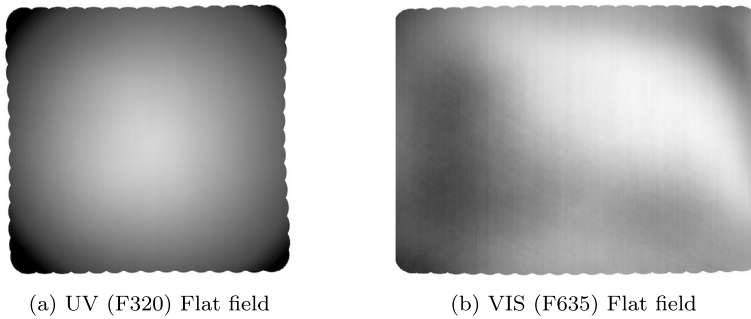
Fig. 10 Sample flat fields for the UV and VIS cameras. The 'scalloping' at the edges is due to the way that the image is collected by rastering an illuminated spot

the spot is scanned over the entire FOV with grid spacing to overlap the spots by 50% or more. The intensity of the source is monitored so that any changes due to source brightness can be removed in processing.

The second method used as a quick 'sanity' check was to illuminate a Spectralon screen that filled most of the FOV and image that.

All of the images obtained from each camera and filter were corrected for dark current.

The median flux over the top hat spot was calculated for each image in a scan and found that for the UV filters, there was a significant decrease in the median spot value between the center spot images at the beginning of the scan and those at the end. Since the laser was stable during the experiment, this "drift" was interpreted as a slow degradation of the UV output of the LED over time, which must be corrected to generate an accurate flat field. For each scan, the "drift rate" was calculated using a linear fit between the first and last spot images taken at the center of the field.

To construct the flat field, each image from the scan is read, a circular mask slightly smaller than the spot size is applied, the "drift" correction is made to all pixels, and the values at each pixel were then summed and divided by the number of samples (files). The resulting flat fields show significant variation across the field-of-view due to optical response (Fig. 10). The UV camera shows strong vignetting with $\pm \sim 30\%$ deviation from the center to the edges in the f220 and f260 filters and $\pm \sim 40\%$ for the f320 filter. There is little vignetting for the visible camera, but there is still $\pm \sim 30$ % spatial variation across the FOV for all three visible filters.

After subtracting the optical response, the pixel-to-pixel RMS deviation across the flat field is $\approx 1.1\%$ in the UV camera and $\approx 0.95\%$ in the visible camera. But note that the RMS deviation for the UV camera is somewhat better in the center of the FOV due to the vignetting. All hot and cold pixels ($> 5\sigma$) were identified. The total fraction hot and cold pixels for each filter is typically less than 0.02% of the illuminated FOV (which is somewhat smaller than the full array size). Most of the cold pixels—and some of the hot ones—appear to be associated with dust on the detector.

After identifying all bad pixels, a flatfield correction image was generated for data processing by inverting the normalized flat field and then setting all bad pixels to 0.

3.3.3 Spectral Radiometry

In order to measure the center-point spectral response of the channels, a fiber-fed collimator was used to illuminate the instrument with a tunable laser source similar to the NIST

CIRCUS system (NIST 2020b). This comprises a Coherent MIRA TiSaphire pumped laser system that provides a tuneable, monochromatic, source from 195–880 nm. The laser is coupled via an optical fiber to a 51 mm Spectralon integrating sphere with 5 mm exit port at the focus of a 457 mm f/5 parabolic collimator. This provides a uniform radiance source with radiance deviations across the beam of <500 ppm RMS.

The EXI instrument is mounted on a two-axis manipulator (yaw and X) to maintain the entrance pupil in the same position in the beam using coordinated moves. To make the measurement first the stage is moved to place the reference detector aperture at the same position in the beam as the entrance pupil. The channel to be measured is then moved into the beam placing the entrance pupil at the same location as where the reference detector measured irradiance. These measurements are made at the center of the FOV and also at four off-axis points in the pitch direction. A beam monitor is used to track any relative changes in the beam intensity between the reference detector and instrument measurements. As the focus of the instrument is not critical for these measurements, they are made in-air.

The initial calibration plan only called for a few wavelengths to be measured over each of the channel bandpasses. However, the measurements did not agree well with the modeled response and showed oscillatory behavior with wavelength within a given channel. This was determined to be due to an etalon formed by the passivation layer at the detector surface. Therefore, to fully characterize the spectral shape of the bandpass more measurements were needed. A second setup was required due to 1) the time it takes to tune and stabilize the laser system at a given wavelength, and 2) changing the wavelength of the laser system in small increments is not always possible. A monochromator was used to make relative measurements of the bandshape, and these measurements were directly tied to the laser measurements (Fig. 11). A McPherson VM502 monochromator with fiber-coupled laser-driven white light source was used. The monochromator exit slit was set to 3 nm FWHM feeding a pair of 76 mm off-axis parabolas (f/10 and f/18). This produces a ~2 mm spot at the center of the EXI channel aperture. The instrument is again mounted on a 2-axis manipulator (yaw and X) to maintain the entrance pupil in the same position in the beam using coordinated moves. To make the measurement the beam from the monochromator was focused on the aperture of the reference detector or EXI so that all the power in the beam is measured. This was to avoid the complexity and light loss associated with generating a uniform irradiance beam across the two apertures. The monochromator was scanned through the desired wavelength range at a constant rate while EXI takes images at a rate of at least 2 images per nm. The scan was then repeated with the reference detector in the beam.

3.3.4 Stray Light Characterization

The goal for EXI was to minimize stray light (ghosts and scatter) to a level that they would be undetectable in a science image, this means that the tricky task of trying to correct for it in analysis is unnecessary. This EXI optical design was based on this principle and measurements at both component, and full instrument level were used to verify that the stray light was below the detection level.

At component level the scattering from the baffles, lenses, coatings, and filters was quantified by measuring the scattered light intensity as a function of angle. The measurement system had a dynamic range $> 1 \times 10^9$.

To assess the effectiveness of the baffles, ray-tracing was used to optimize the design and verified by measuring the scattered light from the baffle assemblies by measuring the signal behind the baffles vs. angle. The Sun (via a heliostat) was used as a source for these measurements.
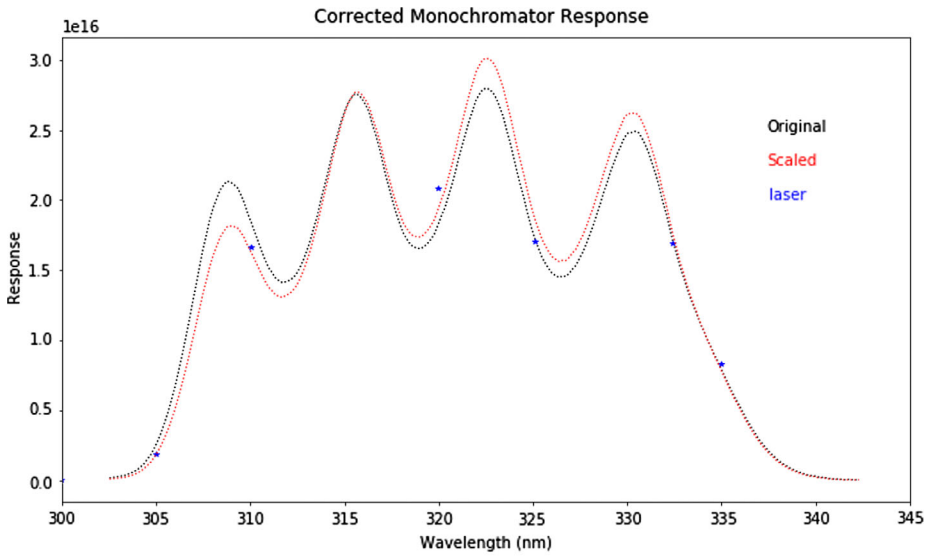
(a) f320
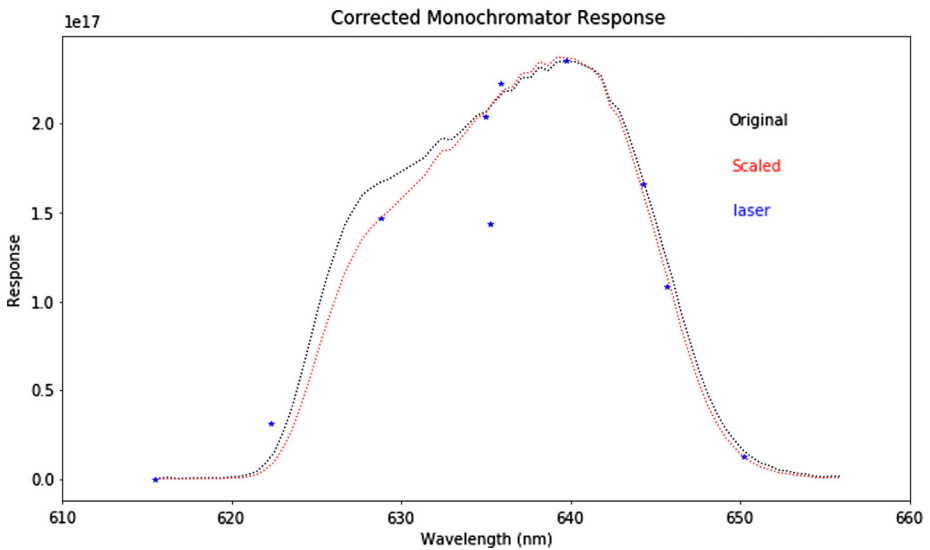
(b) f635

Fig. 11 EXI spectral response for f320(a) and f635(b). The effect of the etalon at the detector surface is especially pronounced in the f320 response curve but is present in all the channels

To verify the results the full instrument was tested by imaging a collimated, occulted source, so that there was no direct illumination of the lens, and again scanning over angle. To be able to detect the scattered light the detector integration time and source intensity were increased. This demonstrated that the infield scatter would not be detectable during an EXI science observation.

Table 6 Summary of the EXI calibration results

Channel	λ_0 (nm) (nm)	FWHM (nm)	Bandwidth (nm)	Band response (ground) (DN nm/J)	ASR_{max} (DN/J)	Uncertainty (%)	Band response (cruise) (DN nm/J)	Uncertainty (%)
f220	249.5	106.6	43.0	4.006×10^{16}	9.311×10^{14}	100.7	3.11×10^{16}	5.3
f260	264.1	48.3	18.9	1.251×10^{17}	6.638×10^{15}	9.2	1.23×10^{17}	2.7
f320	321.3	24.1	19.7	5.805×10^{17}	2.950×10^{16}	5.1	5.35×10^{17}	1.1
f437	437.2	14.2	19.6	N/A	N/A	N/A	2.88×10^{18}	14.9
f546	546.3	15.0	20.2	N/A	N/A	N/A	6.57×10^{18}	17.5
f635	637.7	14.5	17.1	4.117×10^{18}	2.407×10^{17}	2.2	4.13×10^{18}	5.8

λ_0 is the center wavelength, ASR is the Absolute System Response, Band Response $= \int ASR(\lambda)d\lambda$ The response uncertainty (especially for the f220 channel which has a large red leak) is dominated by out of band contributions. Due to time constraints, no ground calibration data was taken for the f437 and f546 channels

Table 7 Predicted sensitivity at Mars for a bright observation: $L_s = 105$, with bright clouds in the UV and bright surface in the visible

Channel	Predicted sensitivity	
	W/nm/pixel	DN/pixel/s
f220	2.331×10^{-15}	9.337×10^{1}
f260	2.334×10^{-15}	2.920×10^{2}
f320	1.052×10^{-14}	6.109×10^{3}
f437	6.867×10^{-14}	1.991×10^{5}
f546	7.410×10^{-14}	2.765×10^{5}
f635	6.692×10^{-14}	2.755×10^{5}

3.4 Summary of Ground Calibration Results

Unfortunately, many circumstances conspired to drastically reduce the amount of time we had to perform system-level characterizations. Though measurements of the detector quantum efficiency (Fig. 23) have been made on sample detectors early in the program, the wavelengths chosen for the tests were too sparse to show the effect of the detector surface passivation etalon. Similarly, reliance on the manufacturer's filter response profiles did not highlight the impact of red-leaks, especially in the f220 filters, and the consequences were not appreciated until results from the system-level characterization were analyzed. Once the issue was identified extra time was used to more fully characterize the f220, f260, f320, and f635 channels, but this was at the expense of having no time to make any measurements of the f437 and f546 channels. The red-leak in the f220 channel is such that there is more signal from out-of-band light than in-band, driving the uncertainty in the measurement so high that the f220 channel has been descoped from routine observations. This was the EXI channel most sensitive to dust, so the dust measurements from EMIRS will be used instead of the EXI measurement. These issues mean that the modeled radiometric performance described in Appendix A bear little relationship to the actual instrument. However, using the measured performance described above, and the modeled imaging uncertainties (scattered light, motion blur, etc.) the combined radiometric uncertainty for EXI is given in Table 6, and the expected sensitivity for Martian observations in Table 7.

3.5 Post Launch Characterization

Planned activities to verify that the performance of EXI has not changed after the launch of EMM will take place shortly after launch, during the cruise-phase, and for the first few orbits of Mars. Observations to track changes in EXI's performance will continue throughout the mission.

3.5.1 Stellar Targets for Alignment Verification

The boresight of the EXI cameras relative to the spacecraft reference frame is measured on the ground using theodolites to measure the offset angles between reference optical cubes on EXI and on the spacecraft. In the visible, a theodolite is configured as an autocollimator so that by translating between the face of the cube facing the boresight direction the collimated light beam can be observed in the VIS camera and so the boresight offset directly measured. This is performed in two orientations so that any sag due to gravity can be accounted for. The offset between the VIS and UV boresights can not be measured using this technique, so the measurements made during the laboratory characterizations of the optical distortion (Sect. 3.2) are used.

To check the alignment post-launch EXI observes stars. With the spacecraft controlled by the star trackers, the relative boresight offsets for the UV and VIS channels can be calculated with respect to the spacecraft pointing. These observations have been completed and the instrument pointing kernels updated. The requirement that the spacecraft inertially point the EXI boresight to within 1° of the target has been easily met, and the current estimate is that the boresight pointing is better than 20′. The stellar images also show that the PSF of the system is very similar to pre-flight measurements. All the light from the stars falls within 1 pixel for the VIS system, and on a few pixels for the UV.

3.5.2 Field Distortion Verification

The first-light images from EXI were of the bright stars in the constellation of Orion. As the geometry is very well known these observations are used to verify that the image distortion has not changed since it was measured on the ground. This provides a very sensitive test that elements in the lens stacks or detector did not shift during transport and launch.

3.5.3 Stellar Targets for Radiance Verification

In order to confirm and update the radiometric ground calibration, observations of the standard stars ηUMa and αLyr were carried out during cruise phase. Both stars were observed with all 6 filters in multiple locations on the detector on multiple dates for a total of 134 and 53 images of αLyr and ηUMa (respectively). Aperture photometry was carried out on each image using the astropy/photutils package after applying a pixel area map correction to account for optical distortion (Sect. 3.2). Note that ηUMa was not detected in the F220 and F260 bandpasses.

In the UV bandpasses, the overall scatter of the flux measurements is generally consistent with the expected noise due to Poisson statistics and CCD performance. The scatter in the fluxes for visible bandpasses, however, is much larger than the CCD uncertainties due to the severe undersampling of the stellar point spread function (PSF), especially at F437 and F546 (the uncertainty in the F546 ηUMa data is artificially small due to the small number of observations obtained in that filter). Due to camera distortion, the PSF is sharper at the center

of the field than at the edges and so the scatter in visible flux measurements is somewhat smaller for observations taken with the star greater than 500 pixels from the center. In order to improve the uncertainty, we excluded any measurements taken with the star less than 500 pixels from the optical axis in the visible.

In the UV, we found that the pixel area map does not accurately correct the flux values, most likely due to uncertainty in the derived distortion coefficients for the UV camera. Hence we opted to exclude any measurements in the UV made outside a few hundred pixels of the optical axis.

The fluxes for both standard stars (Turnshek et al. 1990) were then compared to model fluxes for the given bandpasses using stellar atmospheric models , convolved with the filter curves, in order to determine the radiometric response of the camera at each bandpass (6). The measured band responses for both αLyr and ηUMa are generally consistent within a few percent, with the exception of F546, although we note again that the flux value for ηUMa is based on only a few observations. The F260 and F635 responses agree with the ground values within errors and the F320 response is within 10%. The measured responses for the other filters are generally within 30% of the predicted values. In order to monitor the band responses and improve the measurement errors, αLyr will be observed each quarter during the mission. Images will be obtained in all 6 filters using a 9 point dither pattern in order to mitigate measurement uncertainties due to PSF undersampling.

3.5.4 Flat Field Verification

Various methods will be used to characterize the on-orbit flat field. Some of the stellar measurements (both specifically for EXI and 'ride-along' measurements with Emirates Mars Ultraviolet Spectrometer (EMUS)) will either raster or smear the stellar image across several pixels. As the brightness of the stars will not have changed on the timescale of the measurement this is used to check that the pixel-to-pixel variations have not changed since the pre-launch measurements. Similarly, during the Martian capture orbit, EXI will make measurements of the Martian disk near perigee, when the disk will over-fill the detectors, and the S/C is moving fast. This will again give 'smeared' images that can be used to verify the flat field over the entire detector (*for example,* Shing et al. 2017).

3.5.5 Stellar Targets for Degradation Tracking

Stellar targets (αGru, ηUMa, and αLyr) will be observed throughout the mission to provide degradation tracking. Many of these observations will be "ride-along" observations with the EMUS instrument.

3.5.6 Martian Targets for Degradation Tracking

Throughout the mission targets such as Arabia Terra for the VIS will be used to track any degradation in instrument responsivity as, under similar lighting conditions, these areas are not expected to show significant changes in radiance under low and moderate dust loading conditions. Analogous targets for the UV are more problematic. However, one will attempt to use the residual polar caps when visible in conjunction with near-simultaneous observations by Mars Reconnaissance Orbiter and the Trace Gas Orbiter.

Fig. 12 EXI Concept of Operations. During normal science operations at Mars EXI will take a set of science images (XOS-1) immediately before an EMIRS science observation, and one (XOS-2) immediately afterward
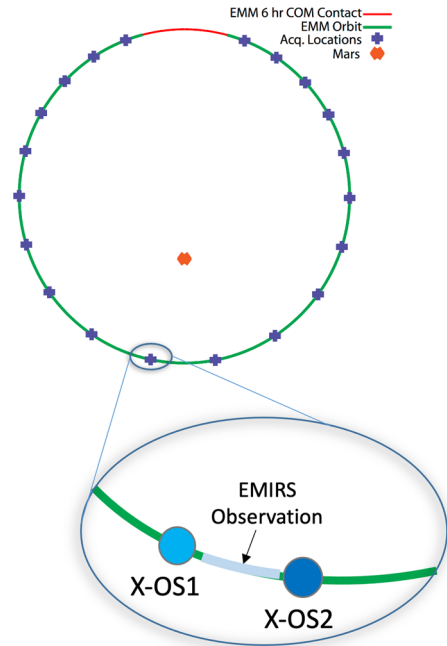
4 Concept of Operations

EXI makes measurements in conjunction with the other two scientific instruments on EMM, the Emirates Mars Infrared Spectrometer (EMIRS) and EMUS. While there is currently no plan to make such observations simultaneously, the EXI planned sequences are typically coordinated with those of the EMIRS instrument (Fig. 12). A similar orchestration with EMUS is not part of the present observational requirements. EXI observations are controlled by Flight Activity Definitions (FADs). These are pre-planned sequences that define all the instrument parameters needed to make a set of observations and simplify the observation planning process.

EXI will be capable of providing observations to fulfill navigation, public relations (PR), and science products. This is accomplished through the use of four standard observation sets (of Mars): two for science observations, one for PR needs, and one for instrumental calibration. During any EXI observation, the spacecraft will provide stable pointing. A typical EXI observation set takes <40 s.

The science observation sets (EXI XOS-1 and -2) include the two bands needed to calculate the ice optical depth and the ozone column abundance, *i.e.,* 320 nm and 260 nm, respectively. In addition, observations in the 220 nm and the 635 nm channel will be taken. These were originally intended to constrain the dust column but a failure of the 220 nm filter to meet the design specifications resulted in a significantly reduced sensitivity to dust in the atmosphere. The 635 nm image remains very useful for tracking discrete dust activity, and the 220 nm is typically included in the data downlink (the savings in data volume has already been incorporated in the observatory data budget). The difference between the XOS-1 and XOS-2 sequences is that the latter uses a higher binning (~64 km per binned pixel). In essence, XOS-2 is designed to capture any regions of the planet observed by EMIRS, but that were not present in the XOS-1 observation (*i.e.,* due to planetary rotation and slight

Table 8 EXI observational strategy

Observation strategy	Observation strategy set
EXI XOS-1 (science)	3 Contemporaneous images
	260 nm, 320 nm, 635 nm
	Incident $< 80°$; emergence $< 70°$
	2×2 pixel binning
	(≤ 0.19 mrad spatial resolution)
	2 dark images (one for each detector)
EXI XOS-2 (science)	4 Contemporaneous images
	220 nm, 260 nm, 320 nm, 635 nm
	Incident $< 80°$; emergence $< 70°$
	16×16 pixel binning
	(≤ 0.49 mrad spatial resolution)
	2 dark images (one for each detector)
EXI XOS-3 (PR)	3 Contemporaneous visible images
	437 nm, 546 nm, 635 nm
	Full resolution (≤ 0.11 mrad spatial resolution)
EXI XOS-4	6 Contemporaneous images
	220 nm, 260 nm, 320 nm, 635 nm, 437 nm, 546 nm
	UV image 2×2 pixel binning
	VIS Full resolution (≤ 0.11 mrad spatial resolution)
	Incident $< 80°$; emergence $< 70°$
	2 dark images (one for each detector)
EXI XOS-5	The observation consists of 4 unbinned images
	(one dark and one flat field for each detector)
	with the door closed and filter in the blank position and 1 unbinned FGPA Test Pattern

change of the spacecraft perspective). This provides the so-called "bookend" observations for EMIRS. Because the EMIRS aperture footprint is on the order of hundreds of kilometers, the higher binning (and lower data volume) are adequate for the purposes of correlation with EMIRS data. The third observation set, XOS-3, focuses on the three visible bands to allow the production of natural color images, primarily anticipated to be used for PR and outreach purposes. The fourth EXI observation set, XOS-4, is a combination of XOS-1 and detector native resolution. Given the focus on calibration, this observation will be conducted once per week. Finally, there is a fifth observation set, but it does not involve Mars. It is also focused on calibration and utilizes an internal LED lamp. Specifically, the observation consists of 4 unbinned images (one bias frame and one stimulus lamp image for each detector. This is done with the door closed and the filter in the blank position. Table 8 summarizes EXI observation sequences.

Table 9 EXI data products

Data level	Data product
Level 0	Binary packets including ancillary data & HK data
Level 1	Raw (uncalibrated) FITS image including ancillary & HK data
Level 2a	Calibrated FITS images with geometry information derived from a reconstructed ephemeris
Level 2b	Calibrated multi-bandpass FITS image, where each bandpass is mapped to a common grid and stacked

Level 3	Atmospheric retrieval products, in geophysical quantities:
	    –Ice optical depth, referenced to 320 nm
	    –Ozone column abundance

5 Data Products: Definition, Availability, and Policy

5.1 Data Products

As discussed above, EXI observation acquires six 12-megapixel images using bandpasses from the mid-UV through red. These images are packetized and downlinked by the spacecraft. Upon reaching the Earth, the data are reassembled and processed through a series of steps that provide an increasing level of suitability for science analysis. The result of each discrete processing step or level results in specific products, as described briefly in Table 9. Starting with Level 1, the data are stored using the Flexible Image Transport System (FITS) format.

5.2 Data Pipeline: Calibration and Retrievals

The raw telemetry (packet) data are received at the Science Data Center (SDC) during scheduled ground-station (NASA Deep Space Network) contacts. This so-called level 0 data is then assembled into EXI images along with their associated metadata. This process includes standard checks for integrity and missing data and the JPEG lossless decompression. This level 1 product represents the raw image, meaning that there are no corrections for instrumental effects. Level 1 products include the ancillary data needed for subsequent processing (*e.g.,* exposure time, spacecraft clock time) needed for subsequent processing. These level 1 images are then processed standard techniques to remove the effects of the instrument (e.g., flat-fielding, bias correction, dark subtraction), producing the level 2 radiometrically and geometrical calibrated product. The latter aspect includes the calculation of photometric angles for each on-disk pixel as well as information such as latitude, longitude, and elevation with respect to a reference surface. Ultimately, the geometry information is calculated twice; the first time using the predicted ephemeris kernels, and ultimately with the reconstructed trajectory kernels. The final step in the processing is that of level 3 or retrieval products. Here, the 260 nm and 320 nm level 2a products are used to derive the water ice optical depth and ozone column density for each pixel that meets certain geometric and quality requirements (i.e., emergence angles less than 70° and incidence angle less than 80°). The algorithms behind the level 3 processing are essentially those that were developed for MARCI (Clancy et al. 2016; Wolff et al. 2019).

Table 10 EXI coverage requirement

Diurnal requirement	In any given span of 10 days, the four three-hour intervals spanning 6 am–6 pm local time are sampled with at least 80% coverage of longitude in:
	$\geq$3 local time intervals for all latitude equatorward of $\pm 30°$
	$\geq$2 local time intervals for all latitude equatorward of $\pm 50°$
	In any given span of 10 days, at least one in the 4 three-hour intervals spanning 6 am–6 pm local time is sampled with at least 50% coverage of the longitudes for all latitude equatorward of $\pm 80°$
Geographic requirement	$\geq$80% of the geographic area of Mars sampled more frequently than every 72 hours
	Latitude $\leq 80°$ sampled more frequently than every 72 hours
Seasonal requirement	Observations over 1 full Martian year
	(Goal: 20 of the 24–15° intervals of L_s sampled)

5.3 Data Completeness and Utilization

The idea of data completeness for EXI considers a spatial dimension and two temporal dimensions (diurnal and seasonal). Because spatial and seasonal coverage are quite straightforward, we focus here on a brief description of the diurnal coverage. The EXI dataset completeness is defined with respect to four 3-hour bins that nominally span between sunrise and sunset (more bins are available during polar summer and fewer during winter). Because of EMM's orbit, this coverage is constructed or "built-up" over a period of 10 days. In other words, systematic day-to-day variability is averaged out (or adds noise, depending on one's perspective) in such a binning scheme. Using this metric, a typical 10-day sampling period offers 80% longitudinal coverage from 6 am to 6 pm local solar time when considering the use of 4 three-hour bins. If one considers only the spatial coverage period, EXI data will sample nearly all longitudes and latitudes in less than 72 hours, thus providing continuous monitoring of moderate-to-large scale dynamical events during the Martian year (*i.e.,* storm fronts, dust events). Table 10 provides a more detailed summary of the EXI coverage and sampling goals (including the diminishing diurnal coverage as one moves poleward).

5.4 Data Availability

It is the intention that all usable mission data from EMM will be released to the public, allowing for access by the international scientific community. There will be no formal proprietary periods associated with any of the EMM data products. Nevertheless, there will be some delays between acquisition and availability of the data on the order of several months (longer during the early part of the mission) so that the processing and data quality can be verified. An interested user can access the Level 1–3 EXI products through the Emirates Space Data Center (ESDC) at sdc.emiratesmarsmission.ae The ESDC, which will physically host the data, is the designated mission archive for all the EMM data in perpetuity (*i.e.,* including the post-mission period). The first release of Levels 1 and 2 science data products will be approximately four-to-five months after the Hope probe reaches the science phase of the mission (*i.e.,* the transition phase from Mars Orbital Insertion to Science Orbit will take several months). This first release of data will include the first three months of science observations. After the initial release, new data will be available on a three-month cadence. The level 3 data releases will lag the level 2 release, at least for the first part of the mission, For example, the level 3 products for a specific three-month observation period will be not be available until 3 months after the release of the associated level 2 products.

Fig. 13 Example JMARS used to overlay EMM-EMIRS Mission Operations Long Duration testing (MOLD) level-0 data overlaid on THEMIS day IR false color image. Similar overlays with EMM and other mission data will provide flexible visualization of multi-mission data
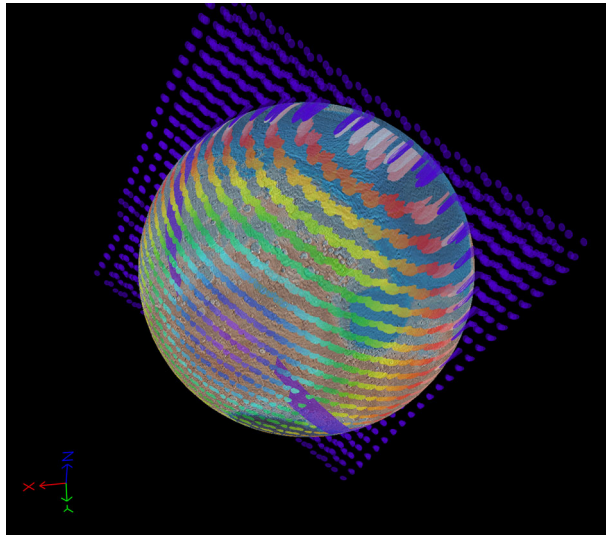
5.5 Data Visualization

To aid in data visualization and integration between the datasets of EXI, EMIRS, and EMUS, the EMM mission is using the JAVA Mission- planning and Analysis for Remote Sensing (JMARS) tool (available from jmars.asu.edu) developed by the Mars Space Flight Facility at Arizona State University (Christensen et al. 2009). JMARS is geospatial software designed to provide mission planning and data-analysis tools to scientists, instrument team members, and the general public. JMARS has been publicly available since 2003, used in over 65 countries, and has currently over 6,000 active users worldwide. It is open-source and is supported for MacOS, Windows, and Linux operating systems. Additionally, JMARS provides free access to data from previous Mars missions such as Mars Global Surveyor, 2001 Mars Odyssey, Mars Reconnaissance Orbiter, Mars Express, and Viking 1 &2 Orbiters. The addition of the EMM mission to the suite of publicly available data available within JMARS environment allows for fast and efficient cross-correlation and interdisciplinary studies between current and previous datasets.

JMARS has a built-in image and vector processing syntax to compare, plot, and blend multiple datasets. Additionally, it can ingest multiple datasets/products to create a single (Fig. 13), registered multilayer image. Creation of profiles (*i.e.,* topographic), contour plots, and extraction of numeric data (i.e., temperature) are tools available for use within the software. Users may also load their own custom maps or data products. For example, one can: load raster files with on-the-fly stretching and colorization; ingest several common vector file formats, and edit such vector data in a map or table format, and use vector processing tools to calculate such as line bearings and area. The JMARS software includes 3D visualization capability, which will be particularly powerful for cross-correlation of the atmospheric datasets of the EMM mission.

6 Mission and Instrument Status

The Hope probe was successfully launched from Tanegashima in Japan on 20 July 2020 at 1:58 a.m. UAE time (19 July 2020, 21:58:14 UTC) and Mars Orbit Insertion was suc-

cessfully accomplished on 9 February 2021. During the Launch and Early Operation Phase (LEOP), EXI instrument checkout activities were all successful with no anomalies. The first light observation was of a star field in the constellation of Orion which was used to assess the pre-launch distortion map. Only very slight changes were noted signifying that there have been no significant shifts during launch. The distortion model (Table 5) has been updated with these results. Radiometric calibration looking at ηUMa, and αLyr (Vega) were taken during the Cruise Phase to verify instrument sensitivity, and will continue to be made during the mission. On 10 April 2021, the science phase of the mission commenced in an orbit of 20,000×42,600 km with an orbital period of 54.5 hours. More information about the mission can be found on the EMM website at: https://www.emm.ae

Appendix A: EXI Imaging and Radiometric Performance Model

EXI is a six-band UV-VIS spectral imager intended for high fidelity monitoring of aerosols in the Martian atmosphere with high radiometric accuracy. The science signal that EXI is to provide is full-disk images of the planet from the EMM spacecraft orbit in the UV and visible red spectral bands listed in Table 3. The images are to have a resolution element sample grid spacing of 10 km or less. Each resolution element is to have radiometric uncertainty of less than 5%. EXI has an additional non-scientific requirement to take high-quality images in the visible red, blue, and green. Assessing the radiometric accuracy of an imager is a somewhat tricky undertaking as crosstalk between adjacent resolution elements can corrupt the signal in an unpredictable manner. Performance can generally be predicted through analysis of the system Modulation Transfer Function (MTF), provided the spatial resolution and spatial frequencies of the science scene are well understood. Due to the novel nature of the EXI science, scene imaging requirements such as relevant spatial frequency content and contrast ratios are not well defined. This has resulted in a somewhat unconventional approach to the instrument design and performance evaluation which can be best described as make it as good as it reasonably can be, then check to see if it is good enough. The good-enough metric is based on previous observations and atmospheric modeling predictions, which envision the instrument as an array of 5% accurate radiometers on a 10 km grid, covering the appropriate bandpasses.

In addition to this, there is a self-imposed requirement that the MTF must notionally have a contrast ratio greater than 0.09 at spatial frequencies limited by the 10 km resolution element made under the assumption that the resolution elements must at least be resolvable (Rayleigh criteria). The purpose of the analysis presented here was to reverse engineer the spatial resolution requirements that EXI needs to meet the science resolution and radiometry goals. Section A.1 evaluates the spatial resolution performance of the EXI design and shows that it meets the MTF requirements. Section A.2 uses simulated science images with relevant spatial frequency content to assess the radiometric performance of the design.

A.1 System-Level Spatial Resolution

A.1.1 Approach

The effect of imaging system performance on a scene can be modeled by the convolution of a scene, $d(x, y)$, with the system impulse function, $h(x, y)$

$$f(x, y) = d(x, y) * h(x, y). \tag{5}$$

Table 11 Maximum FOV and spatial resolutions needed to meet the 10 km, 70° emergence angle requirements. The FOV number includes a worst-case orbit and navigation error

Position in orbit	FOV half angle of 70° emergence limit	Spatial frequency for 10 km
Periapsis	8.98°	45 cyc/mm
Apoapsis	4.94°	90 cyc/mm

This is most easily calculated as a multiplication in the Fourier domain:

$$F(u, v) = D(u, v) H(u, v). \tag{6}$$

$H(u, v)$ is the system-level optical transfer function (OTF) for spatial frequencies u and v. In this manner, the full system transfer function can be expressed as a multiplication of several subsystem transfer functions. For the analysis here, the system OTF is split into 3 parts, specifically optical, detector, and spacecraft motion:

$$H(u, v) = H_{opt}(u, v) H_{det}(u, v) H_{motion}(u, v). \tag{7}$$

Throughout the analysis here, the MTF (MTF = |OTF|) is used rather interchangeably with the OTF as the phase function is at most a constant offset resulting from a Fourier domain shift and generally has no impact on the optical performance here.

The spatial resolution requirements are for EXI to have 10 km resolution elements with MTF > 0.09 for Mars emergence angle >70°. The extremes of observing are at periapsis where a 10 km resolution element has a spatial frequency of 45 cyc/mm, and apoapsis with 90 cyc/mm.

MTF of EXI Optics

The EXI optics, particularly the UV channel, are generally not diffraction-limited across the full observational FOV. Limited glass choices restricting the design space resulted in a significant amount of residual aberrations, primarily chromatic and field curvature. As such, this analysis uses a raytrace derived PSF model to calculate the optical MTF and account for variations across the FOV. The MTF sampled at the apoapsis FOV limit from Table 11 are shown in Fig. 14.

Since the as-built performance will undoubtedly be degraded from the designed model, the MTF of the toleranced optical system is used. A sensitivity analysis was used throughout the design process to limit manufacturing specifications to industry-standard precision optical tolerances or coarser. A Monte Carlo tolerancing was then performed to gauge the performance of the as-built system using these tolerances. The analysis here uses a system derived in the Monte Carlo simulations that has MTF performance approximately two standard deviations below the nominal case. The MTFs for these toleranced optical systems vs. field of view are shown in Fig. 15.

Detector Pixel Array

The detector to be used at the focal plane in EXI is a 3072×4096 CMOS array with a 5.5 μm pitch and 42% fill factor. The rectangular shape of the pixels in the array is modeled as a *rect* function that is convolved with a periodic *comb* sampling function, given by

$$h_{det}(x, y) = rect(a_{det}x, \ a_{det}y) * comb(p_{det}x, \ p_{det}y)) \tag{8}$$

Fig. 14 Optical MTF for the four science filter channels at the apoapsis FOV limit (4.94°)
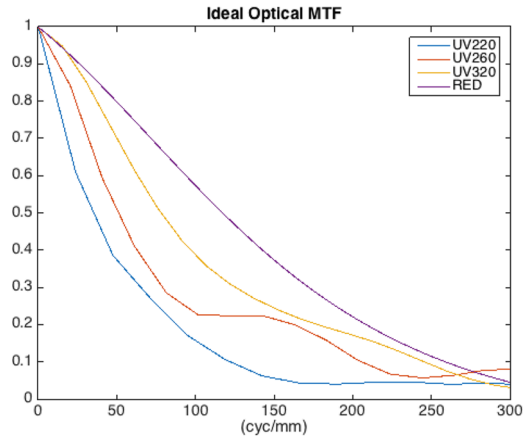
with

$$rect(a_{det}x,\ a_{det}y) = \begin{cases} 1 & |x, y| < \frac{a_{det}}{2} \\ \frac{1}{2} & |x, y| = \frac{a_{det}}{2} \\ 0 & \text{otherwise} \end{cases} \tag{9}$$

and

$$comb(p_{det}x,\ p_{det}y) = \sum_{m} \delta((x, y) - mp_{det}) \tag{10}$$

Here $a_{det} = 3.6$ μm is the width of the pixel active area that is assumed to be rectangular, and $p_{det} = 5.5$ μm is the detector pixel pitch, and x and y are spatial positions on the focal plane with the origin at the center. The transform MTF of the detector array is given by:

$$H_{det}(u, v) = sinc(a_{det}u,\ a_{det}v)\frac{1}{p_{det}}\sum_{m}\delta((u, v) - m\frac{1}{p_{det}}) \tag{11}$$

This is plotted in Fig. 16. Also plotted are manufacturer provided measurements of the MTF, as well as a hypothetical 100% fill factor MTF.

The detector is Nyquist limited at spatial frequencies greater than the cutoff $1/p_{det} = 181.8$ cyc/mm meaning that any spatial content in the image above this cutoff will be aliased to lower frequencies and contribute to the error signal. Since the fill factor is less than 100%, the pixel spatial frequency bandwidth $1/a_{det} = 278$ cyc/mm is very oversampled relative to the sampling period and could lead to picket-fencing errors, although the optical cutoff is less than this so shouldn't be an issue. This is further complicated by the operational plan to bin pixels 2×2 to lower data volume, which also lowers the sampling cutoff to $2/p_{det} = 90.9$ cyc/mm.

Spacecraft Motion

During EXI observations the spacecraft will be 3-axis stabilized and pointed so that the EXI boresight vector is NADIR fixed. Orbital and random motion of the spacecraft platform relative to the NADIR ground scene will cause smearing of the acquired image.
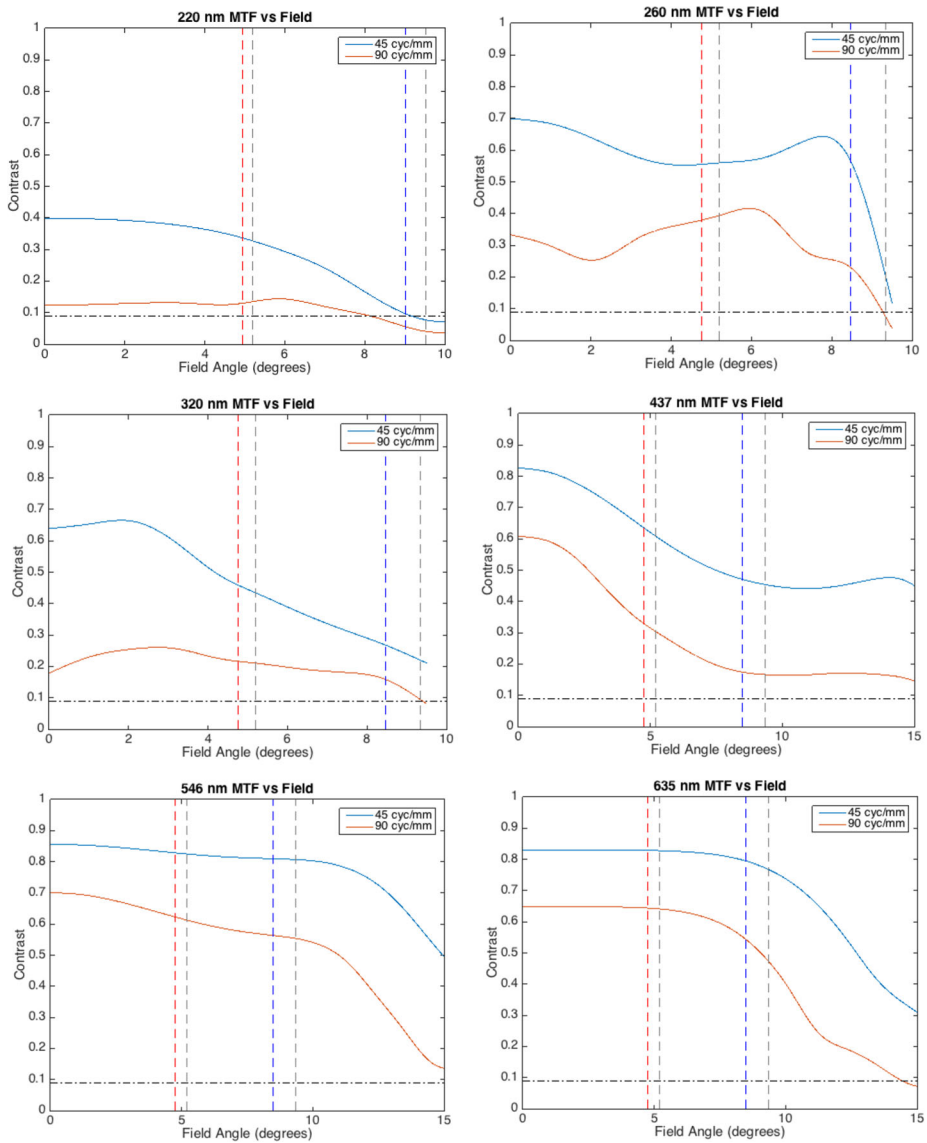
Fig. 15 MTF vs. Field Angle for the toleranced optical system. Periapsis case (blue line) and periapsis FOV limit (blue dash). Apoapsis case (red line) and apoapsis FOV limit (red dash)

Time integration ground smear is a simple linear translation and is modeled by a *rect* function. Assuming motion in the x-direction:

$$h_{smear}(x, y) = rect(a_{smear}x) \tag{12}$$

with smear OTF of:

$$H_{smear}(u, v) = sinc(\pi a_{smear}u) \tag{13}$$

Fig. 16 MTF of the CMV1200 detector focal plane. CMOSIS provided measurements of the MTF made by another customer and the details of the measurements and their associated uncertainties are unknown. As such, it is taken as reference only
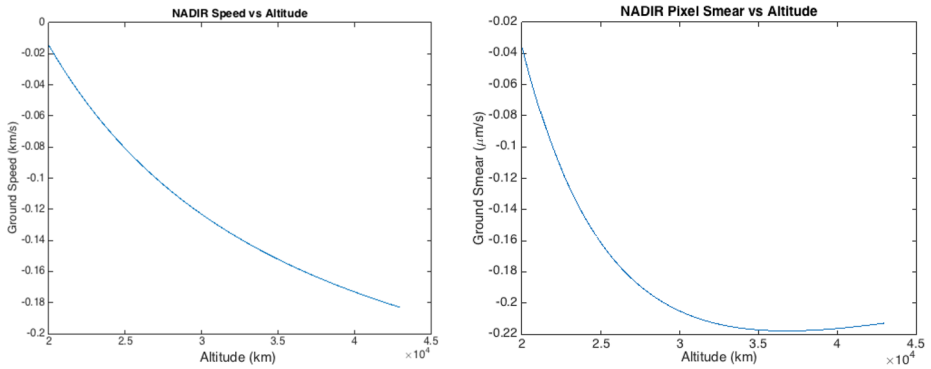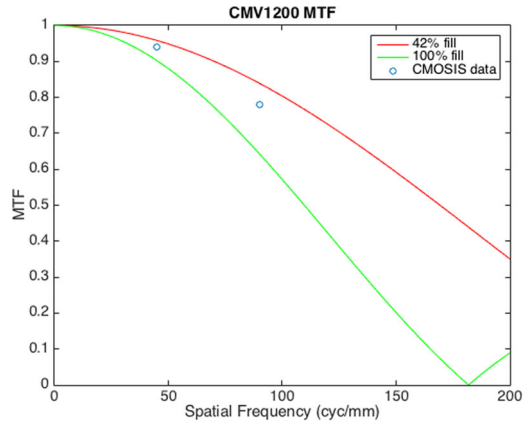
Fig. 17 (left) Spacecraft relative NADIR ground speed, accounting for orbital motion and planetary rotation. (right) Smear motion on the detector, as imaged through the EXI optics

The relative motion of the EMM spacecraft is quite low at NADIR, dropping to nearly zero at periapsis rising to -0.18 km/s at apoapsis, shown in Fig. 17. At the focal plane, this translates to approximately -0.22 μm/s of image ground smear. Given the maximum integration time of 380 ms, shown later in Table 11, $a_{smear} \leq 0.08$ μm.

Jitter is random motion modeled by the central limit theorem as a Gaussian distribution with an RMS displacement σ about each of the three axis. EMM ADCS modeling predicts a broad spectrum jitter on all three axis of $\alpha < 4''$ RMS over 3 s. If the boresight vector is in the z direction, the x and y jitter displacement seen through the optical system at the focal plane is described as:

$$h_{jitter-xy}(x, y) = \exp(-\frac{x^2 + y^2}{2\sigma^2}) \tag{14}$$

with RMS displacement $\sigma = \alpha f \approx 1$ μm. The corresponding OTF is then:

$$H_{jitter-xy}(u, v) = \exp(-2\pi\sigma^2(u^2 + v^2)) \tag{15}$$

Jitter about the z-axis is similar to x-y except that it is a rotation rather than x-y translation of the image. The displacement magnitude of the rotation σ_φ changes with distance from the

Fig. 18 The MTF of spacecraft motion. Jitter about the x-y axes, while marginal, most significantly affects the MTF. Ground smear due to orbital motion during image capture and jitter about the boresight axis are negligible
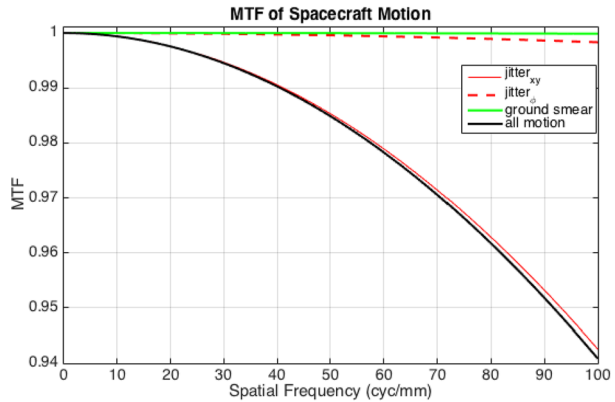
Table 12 Full optical system MTF. Margin the percentage over the Rayleigh criteria target MTF of 0.09

Channel	Apoapsis (90 cyc/mm at 4.84°)					Periapsis (45 cyc/mm at 8.98°)				
	Toleranced Optical MTF	Sensor MTF	SC Motion MTF	System MTF	Margin (%)	Toleranced Optical MTF	Sensor MTF	SC Motion MTF	System MTF	Margin (%)
f220	0.13	0.84	0.95	0.11	17.3	0.10	0.96	0.99	0.09	5.2
f260	0.20	0.84	0.95	0.16	73.3	0.14	0.96	0.99	0.13	45.2
f320	0.13	0.84	0.95	0.10	15.8	0.18	0.96	0.99	0.17	86.1
f437	0.29	0.84	0.95	0.23	159.9	0.43	0.96	0.99	0.41	352.7
f546	0.58	0.84	0.95	0.47	419.1	0.77	0.96	0.99	0.73	707.1
f635	0.61	0.84	0.95	0.49	442.7	0.73	0.96	0.99	0.69	663.3

center of the FOV by:

$$\sigma_\varphi = \alpha\sqrt{x^2 + y^2} \tag{16}$$

and is in a direction orthogonal to the radial. The OTF $H_{jitter-\varphi}$ changes with field position, being unity at boresight (zero effect on the MTF), and is worst at the edge of the field.

All three spacecraft motion MTFs are shown in Fig. 18 for the worst-case disturbances which occur in the f220 channel at apoapsis. Rotational jitter and ground smear are quite benign, with x-y axis jitter having the most significant effect.

A.1.2 Combined System MTF

The full MTF of the imaging system is given by the multiplication of all component MTFs. Specifically:

$$H_{system} = H_{optics} H_{det} H_{smear} H_{jitter-\varphi} H_{jitter-xy}. \tag{17}$$

H_{system} is plotted vs. FOV for the six filter bandpasses in Fig. 19, and is listed in Table 12 along with the contributing subsystem MTFs. All meet the imposed 0.09 MTF with margin, although the f220 bandpass is close.
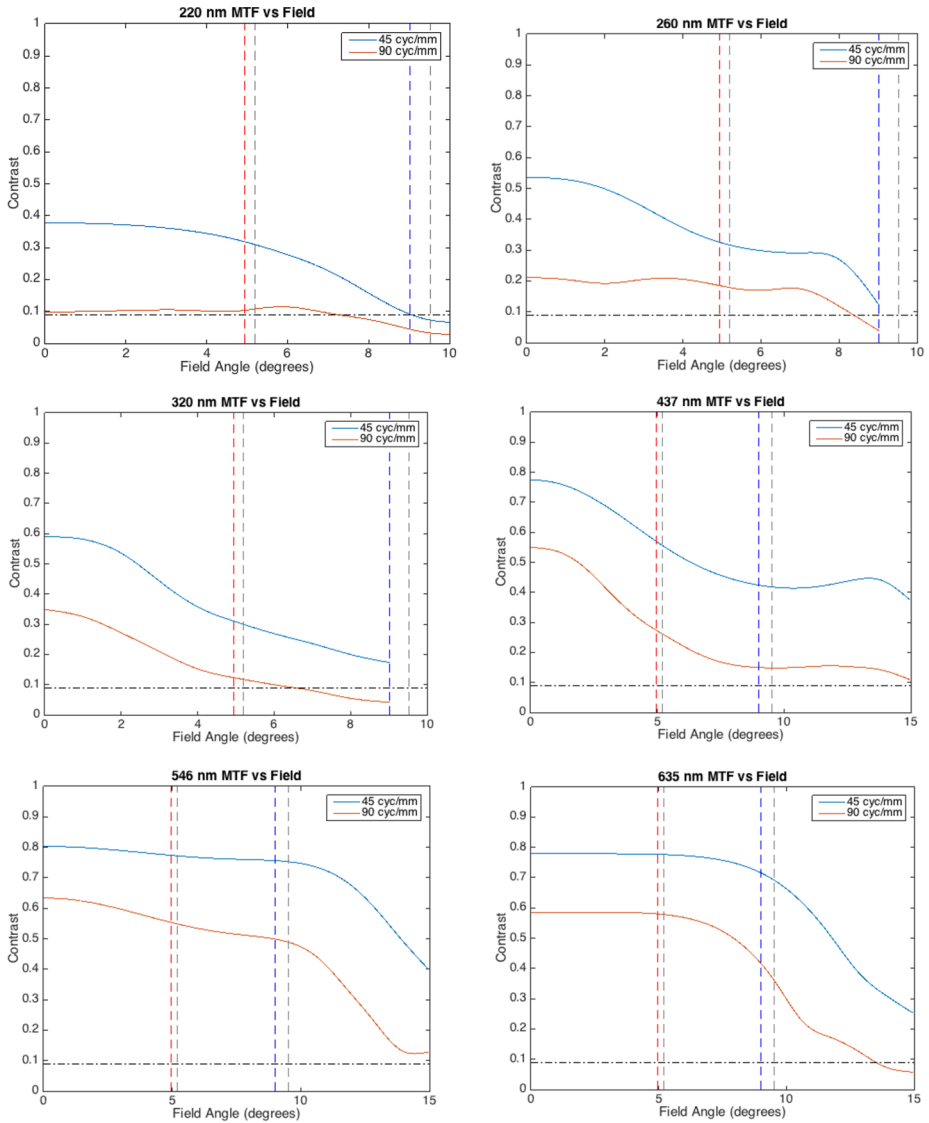
Fig. 19 Full system MTF vs. FOV for each spectral channel. Periapsis case (blue line) and periapsis FOV limit (blue dash). Apoapsis case (red line) and apoapsis FOV limit (red dash)

A.2 Radiometric Performance and Budget

Assessing the radiometric performance of an imaging system can be somewhat tricky. The most direct approach is to use the MTF of the system. The error function metric of the system is then given by 1-MTF for all spatial frequencies. Given the exploratory nature of the EXI science, the spatial frequency content and associated contrasts of the scene to be observed are not well defined, particularly with the radiometric accuracy that EXI hopes to deliver.
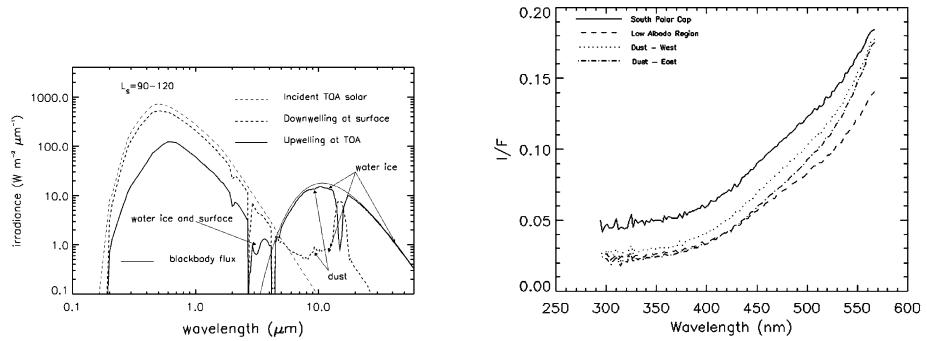
Fig. 20 Mars spectral irradiance near aphelion. Radiance factor I/F, where I is the observed radiance from Mars and πF is the solar spectral irradiance at the top of the Martian atmosphere at the time of the observations (Wolff et al. 2017)

A.2.3 EXI Signal Estimate

The following will investigate the approximate worst-case situations to derive a baseline signal estimate and signal-to-noise rather than a thorough analysis since there are several unknowns such as detector QE for the flight lot, and the as-built UV filter transmissions. From this estimate, an uncertainty budget is developed to access the imaging performance in the next section. Science signal uses measurements of Mars at aphelion for the weakest expected signal.

First some nomenclature:

A_D: detector area, or single pixel area [m^2]

t: Detector integration time [s]

Q_D: Detector quantum yield [e^-/photon]

G_D: Detector gain [e^-/DN]

$R_D(\lambda)$: Detector responsivity [DN/W/pixel]

T_{Lens}:   Optical system transmission [unitless]

T_{Filer}:   Filter transmission [unitless]

H_0:   Spectral irradiance of the observed scene [W/m^2/μm]

H_D: Spectral irradiance at the detector [W/m^2/μm]

N_0:   Spectral radiance of the observed scene [W/m^2/sr/μm]

N_D: Spectral radiance at the detector [W/m^2/sr/μm]

d: Lens aperture diameter [mm]

f: Lens effective focal length (EFL) [mm]

$f/\#\ (=f/d)$: Lens optical f-number [unitless]

The Martian spectral irradiance was provided by Wolff et al. (2017) shown in Fig. 20. Mars reflectance measurements for $L_S = 90$–120 was chosen as it is near aphelion and will represent the dimmest signal EXI will need to see. Assuming that the surface irradiance is Lambertian, the observable radiance from Mars is:

$$N_0^{\text{Mars}}(\lambda) = \frac{H_0(\lambda)}{\pi} \tag{18}$$
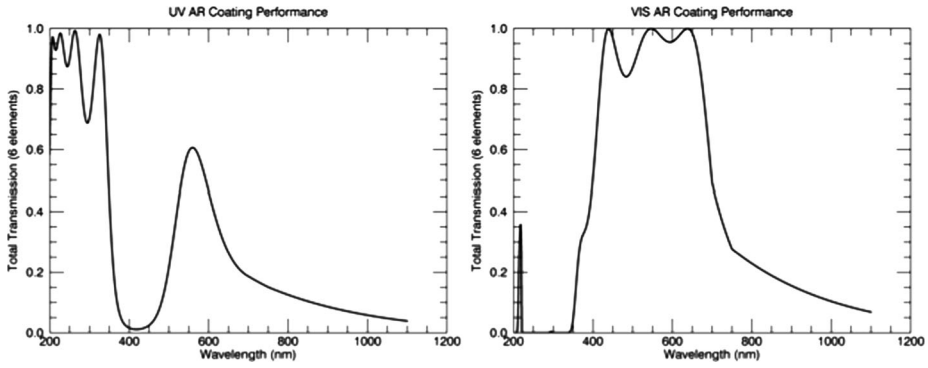
Fig. 21 Transmission coefficient, T_{Lens}, for both UV (left) and VIS (right) channels derived from measured witness samples
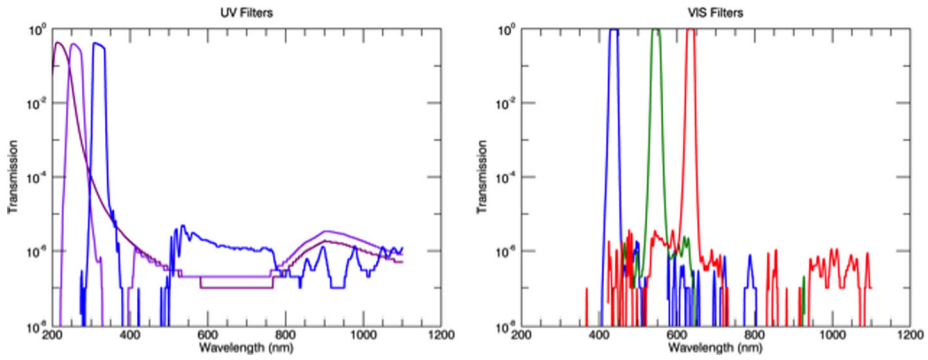
Fig. 22 Modeled filter transmission spectra for the UV filters, provided by Materion-Barr. Measured transmission for VIS filters, provided by Perkins Precision Developments

The radiance through the optical system, at the detector (focal plane) by conservation of radiance is:

$$N_D(\lambda) = T(\lambda)N_0(\lambda) \tag{19}$$

where $T = T_{Lens}T_{Filter}$ is the transmission spectrum of the lens and filter optics. The glasses chosen for the lens elements have transmission $> 99\%$ for each spectral band (Schott (2020), Corning (2020)), so T_{Lens} should be dominated by reflection losses at the vacuum-glass interfaces. Anti-reflective coatings designed for EXI have been measured to be $\lesssim 0.5\%$ per interface. The total T_{Lens} for both the UV and VIS lens stacks are shown in Fig. 21. Modeled and measured filters are shown in Fig. 22.

The spectral irradiance on the detector, H_D, is the radiance N_D that is within the solid angle of the exit pupil of the optical system

$$H_D(\lambda) = T(\lambda)N_0(\lambda)\frac{\pi(\frac{d}{2})^2}{f^2} \tag{20}$$
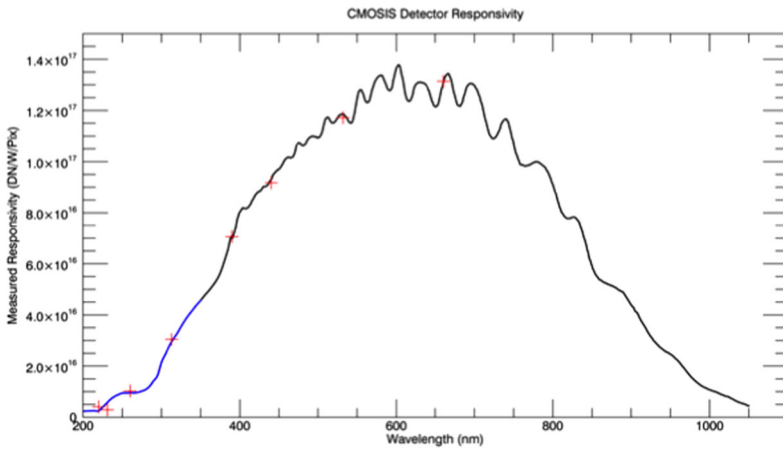
Fig. 23 Measured responsivity of the CMOSIS CMV12000 detector. Measurements from the vendor (black line) and at LASP (red crosses)

Putting this together, the spectral irradiance in the image plane is given by:

$$H_D(\lambda) = \frac{\pi T(\lambda) N_0(\lambda)}{4(f/d)^2} \qquad (21)$$

and the total irradiance for each filter passband is $H_D(\lambda)$ integrated over the band:

$$H_D(\lambda) = \frac{\pi}{4(f/d)^2} \int_\lambda T(\lambda) N_0(\lambda) d\lambda \qquad (22)$$

The number of photoelectrons generated in a single pixel, assuming 1:1 conversion, is given by:

$$M_{pe} = \frac{A_D t}{hc} \int_{\lambda_1}^{\lambda_2} Q_D(\lambda) H_D(\lambda) \lambda d\lambda \qquad (23)$$

Given the detector full well of 54,000 e^- and gain 12.333 e^-/DN, the signal conversion to the 12-bit digital number is listed in Table 13.

The EXI team tested commercially available versions of the CMOSIS CMV12000 detector to get an understanding in advance of the performance of this device. The measured responsivity and typical curve from the datasheet are shown to match quite nicely in Fig. 23. The noise signal is dominated by shot noise, given by $\sigma_{shot} = \sqrt{(M_{pe})}$.

A.2.4 Sources of Error and Budget

The total uncertainty budget for EXI, σ_{total}, can be expressed as the RSS of the individual noise sources:

– Imaging (PSF, scatter, jitter. ground smear)
– Optical calibration (lens and filter transmission, aperture area)
– Detector (QE, fill factor correction, gain, non-linearity correction, timing, shot noise, dark noise, and read noise)

Table 13 EXI signal estimates for binned 2×2 science pixels. Integration time was chosen to set the detector signal level at 75% of full well in anticipation of loss through charge diffusion. Results of detailed testing may allow for the use of more of the dynamic range which should increase the SNR

Channel	Signal (DN/s)	Integration Time (ms)	SNR 2×2 pixel binning
f220	8.00×10^3	380	50.0
f260	5.96×10^4	51	50.3
f320	6.80×10^5	4.5	50.5
f437	1.60×10^5	1.9	50.3
f546	1.22×10^7	0.25	50.3
f635	7.68×10^6	0.4	50.3
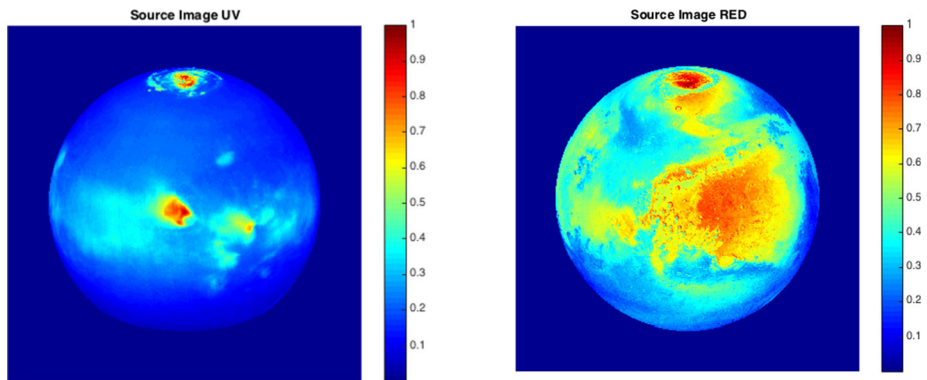
Fig. 24 Representative science imagery. This was created from a large number of MRO-MARCI 320 nm (left) and 653 nm (right) images. The resolution is 2 km/pixel. Units are I/F

– FOV correction
– Navigation/Pointing knowledge
– Solar spectral input
– Degradation knowledge

Estimations for these uncertainties and the RSS totals are listed in Table 14.

A.2.5 Image Simulation

The results in Table 14 sum up the various back-end uncertainties in calibration, electronics, and reduction that are carried by each resolution element. What remains is to ascertain the systems ability to reproduce a scene faithfully enough so that the total error does not exceed the allotted 5%. Specifically, the total error in the reproduction should be less than the imaging uncertainty budget listed in Table 14. Imaging performance is simulated here by performing the convolution of representative science imagery with the system impulse response function explained in Sect. A.2. The pixel-to-pixel fractional error in the reproduction is then used to gauge the imaging uncertainty.

Representative imagery for simulations of the UV and VIS performance are shown in Fig. 24. These are composite images assembled from data from the MRO-MARCI instrument f320 band (UV) and f653 band (VIS). The f320 image is from a period when Mars was near aphelion having clouds in the atmosphere and a north polar cap to provide a stressing

Table 14 RSS modeled uncertainty estimates and budget allowance for imaging errors such as poor MTF, scatter, and platform (spacecraft) stability

Uncertainty Source		Channel					
		f220	f260	f320	f437	f546	f635
Optic	Lens and Filter (T vs. λ)	0.01	0.01	0.01	0.01	0.01	0.01
Detector	QE	0.011	0.011	0.01	0.007	0.005	0.005
	Timing	0.005	0.005	0.005	0.005	0.005	0.005
	Gain and non-linearity	0.01	0.01	0.01	0.01	0.01	0.01
	Science pixel SNR	0.02	0.02	0.02	0.02	0.02	0.02
Data Reduction	FOV correction	0.01	0.01	0.01	0.01	0.01	0.01
	NAV uncertainty	0.005	0.005	0.005	0.005	0.005	0.005
	Solar Spectrum	0.012	0.012	0.01	0.005	0.005	0.005
	Degradation Uncertainty	0.001	0.001	0.001	0.001	0.001	0.001
Non-imaging uncertainty total		0.032	0.032	0.031	0.029	0.028	0.028
Imaging uncertainty budget		0.039	0.039	0.039	0.041	0.041	0.041

dynamic range case. This is used as the simulation input for all three UV bandpasses, despite that — the f220 and f260 scenes should have much lower contrasts and spatial frequency content, it is useful for the evaluation of the optical system. The 653 nm band image used for the f635 simulation shows typical high spatial frequency content and high contrast areas.

The PSF used is from a rigorous non-sequential raytrace that includes scattering, ghosting, and diffraction for the full optomechanical path (Fig. 25. These were then convolved with the spacecraft motion and detector functions to obtain a full system-level impulse response.

Image simulations were performed by a numeric Fourier domain convolution using Matlab's 2-D FFT. The simulated images shown in Fig. 26 appear on inspection to be fairly faithful reproductions without any obvious blurring or artifacts. The more subtle errors can be better seen in the fractional error images, shown in Fig. 27. The UV channel shows significant scatter, particularly on the deeper UV bands, which appears as a background glow. Larger errors are also seen in the high contrast areas of the polar cap and equatorial clouds, caused by the lower MTF of the UV channels. Similarly, the RED image also has errors that are well correlated with high contrast areas in the source image.

The fractional error for each simulation, both at periapsis and apoapsis, was plotted in histograms of pixel count vs. fractional error. The sum of pixels that exceeds an error threshold set by the imaging uncertainty budget from Table 14 are listed in Table 15. While these sums for each are arguably quite low, the imaging error for these pixels violates the 5% radiometric accuracy requirement. The EXI science team has asserted from the beginning that it is not expected for EXI to meet the 5% requirement across the full surface of the planet. High contrast, high spatial frequency content areas such as crater rims and cloud edges are assumed to be problematic and intended to be neglected in the data. This suggests that post-processing of EXI images will need to include a map of the local derivative to flag these regions as potentially problematic, and that the requirement may need to be amended to properly express what was intended.
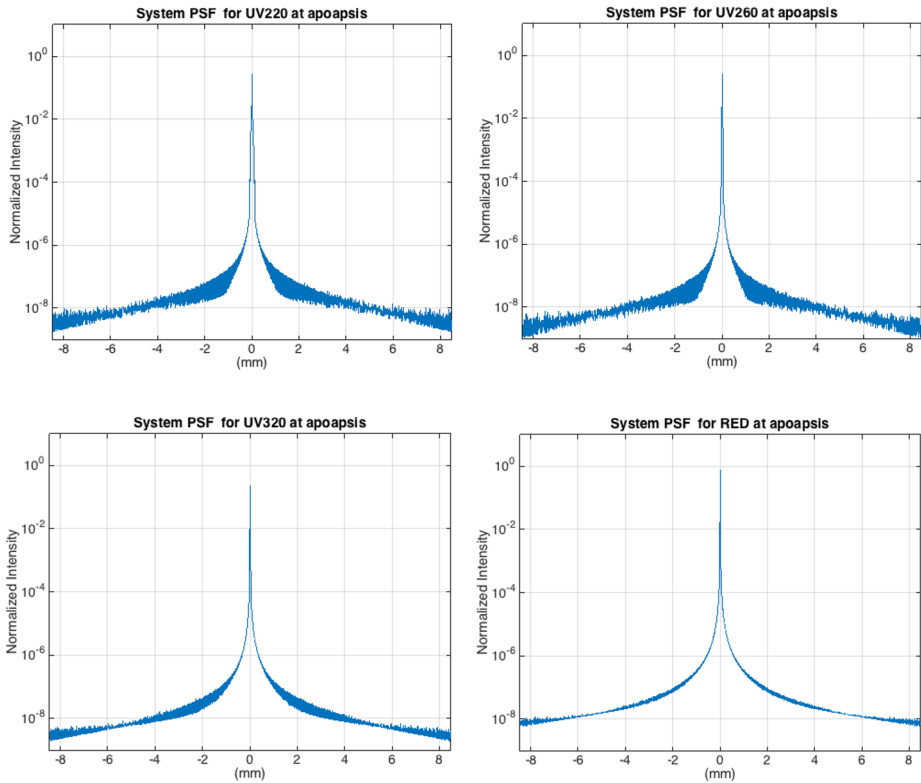
Fig. 25 System-level point spread functions for the four science channels. Since imaging performance degrades with FOV due mainly to field curvature aberration, a PSF was calculated at the FOV observational limit 4.94° at apoapsis, and 8.48° for the periapsis simulation

Table 15 Summary of image simulation results. Shown are the fraction of pixels in the reconstructed image that have a fractional error greater than the allotment in the uncertainty budget

Channel	Imaging Uncertainty Budget	Fraction of pixels with error > Imaging Uncertainty Budget	
		Periapsis	Apoapsis
f220	0.0385	8.20×10^{-4}	4.00×10^{-3}
f260	0.0385	1.71×10^{-5}	1.29×10^{-3}
f320	0.0394	0.00	7.56×10^{-5}
f635	0.0412	7.53×10^{-5}	7.02×10^{-4}

A.2.6 Image Gradient Limiting

As a demonstration of the effect that this can have on the pixel count that exceeds the required uncertainty limit, a gradient map was calculated for the source images. While many methods of calculating local gradients in the source images are possible, the central difference gradient is used here for its speed and simplicity:

$$\frac{dI}{dx} = \frac{I_{x+1} - I_{x-1}}{2} \tag{24}$$
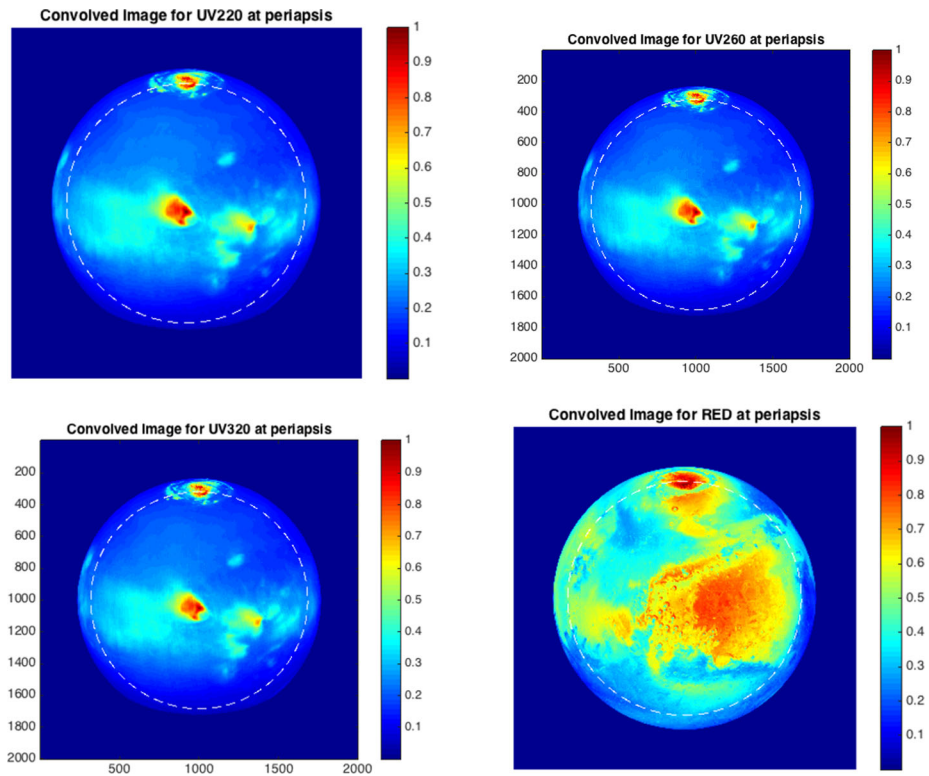
Fig. 26 Simulated science images generated by convolution with the derived system PSF for each science channel. The white dashed line demarks the 70° emergence observation boundary

$$\frac{dI}{dy} = \frac{I_{y+1} - I_{y-1}}{2} \tag{25}$$

The magnitude of the gradient for the UV and red source images is shown in Fig. 28. This gradient mapping was applied to the simulated images from Fig. 26 to flag regions with a local gradient higher than 0.02, shown in Fig. 29 and Fig. 30. The error summary in Table 16 shows that gradient limiting greatly reduces the number of pixels that violate the uncertainty threshold, although high uncertainty pixels still exist.

The value of the gradient was chosen somewhat haphazardly, picking a value that reduced errors without removing too much detail from the images. The choice of an actual gradient threshold, or whether to use on at all, is a task for the science team to decide upon.

Appendix B: Acronyms

ADCS   Attitude Determination and Control System
AIM   Aeronomy of Ice in the Mesosphere spacecraft
ASR   Absolute System Response
ASU   Arizona State University
CCP   Contamination Control Plan
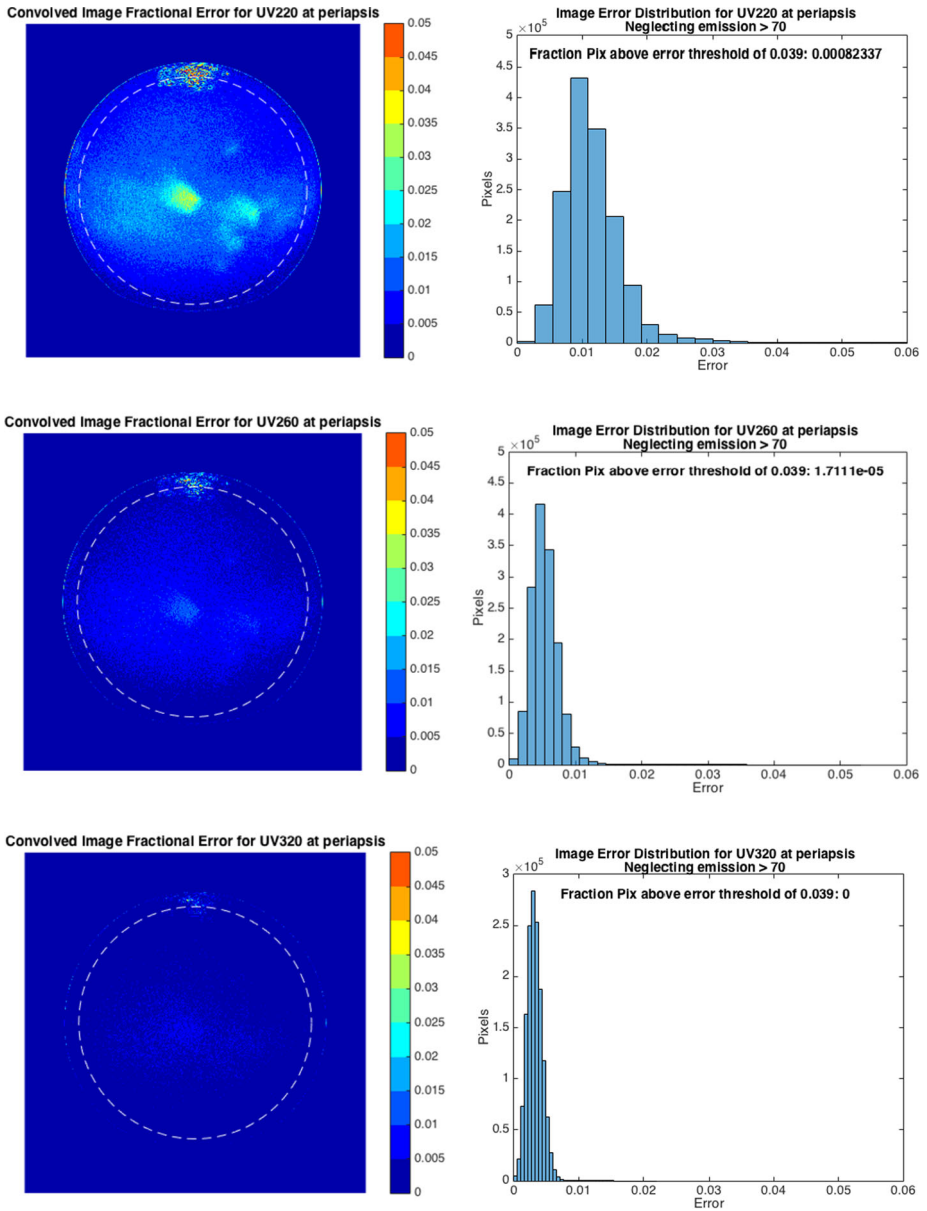
Fig. 27 Fractional errors from representative science image simulations for the four science channels

CDS	Correlated Double Sampling
CIPS	Cloud Imaging and Particle Size experiment
CIRCUS	Spectral irradiance and radiance responsivity calibrations using uniform sources
CMOS	Complementary Metal Oxide Semiconductor
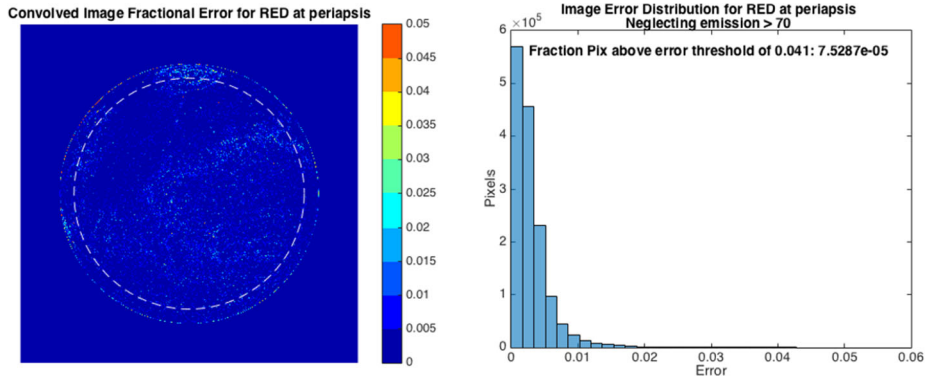
Fig. 27 (*Continued*)
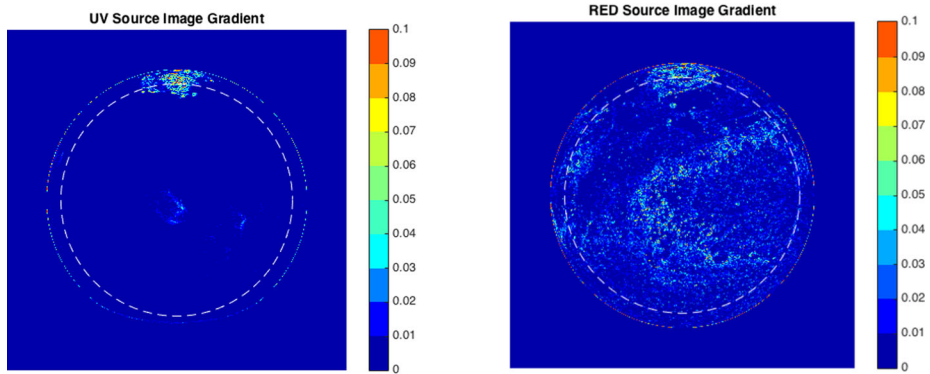
Fig. 28 Magnitude of the local gradient of the UV and red source images. The UV image is fairly flat in intensity, having large intensity gradients only at the polar cap and at cloud edges. The red (f635) image has numerous high intensity gradient regions, mainly at crater edges and other topographical features

Table 16 Reprocessed results from Table 15 to also exclude pixels with local gradient > 0.02

Channel	Imaging Uncertainty Budget	Fraction of pixels with error > Imaging Uncertainty Budget			
		Periapsis		Apoapsis	
		Full Data	Gradient < 0.02	Full Data	Gradient < 0.02
f220	0.0385	8.20×10^4	2.70×10^4	4.00×10^4	8.00×10^4
f260	0.0385	1.71×10^4	3.42×10^4	1.29×10^4	1.42×10^4
f320	0.0394	0.00	0.00	7.56×10^4	1.18×10^4
f635	0.0412	7.53×10^4	8.21×10^4	7.02×10^4	6.62×10^4

CNES	Centre National d'Études Spatiales
ConOps	Concept of Operations
CSTOL	Colorado System Test and Operations Language
CU	University of Colorado
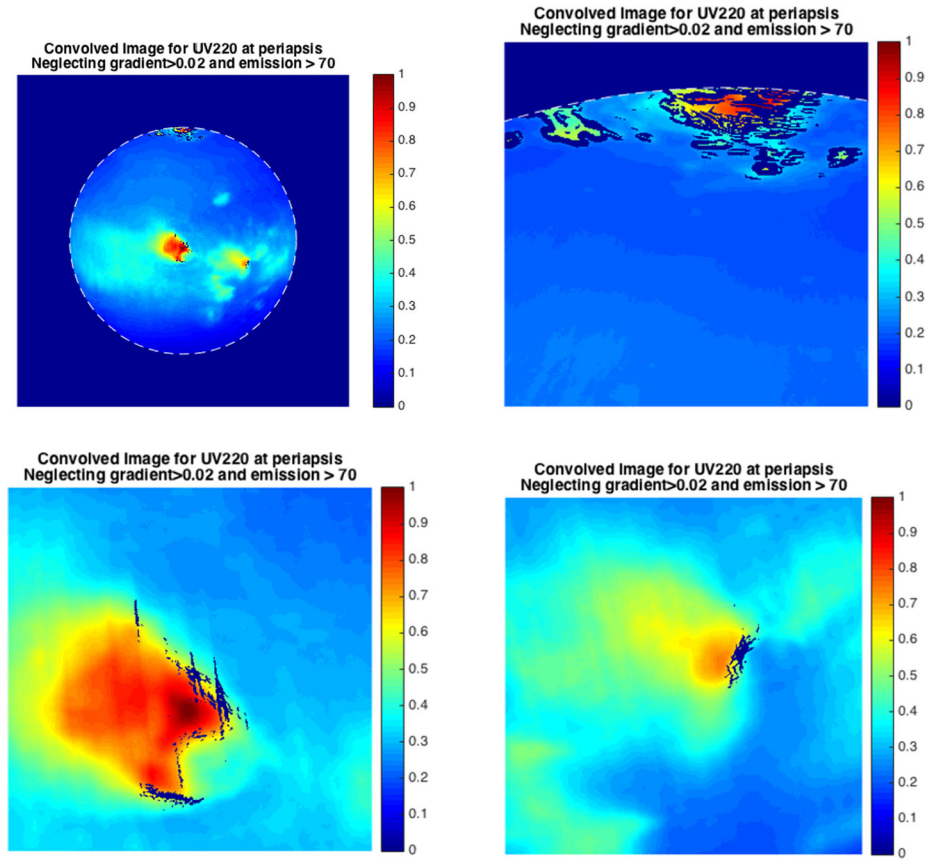
Fig. 29 Reprocessed results from Fig. 26, setting pixels with local gradient >0.02 to 0

DC   Direct Current
DDR   Double Data Rate
DPA   Destructive Physical Analysis
Ebox   Electronics Box
EDAC   Error Correction and Detection
EM   Engineering Model
EMC   ElectroMagnetic Compatibility
EMI   ElectroMagnetic Interference
EMIRS   Emirates Mars Infrared Spectrometer
EMM   Emirates Mars Mission
EMUS   Emirates Mars Ultraviolet Spectrometer
ESDC   Emirates Space Data Center
ESIM   Electrical Simulator
EUI   Extreme Ultraviolet Imager
EXI   Emirates eXploration Imager
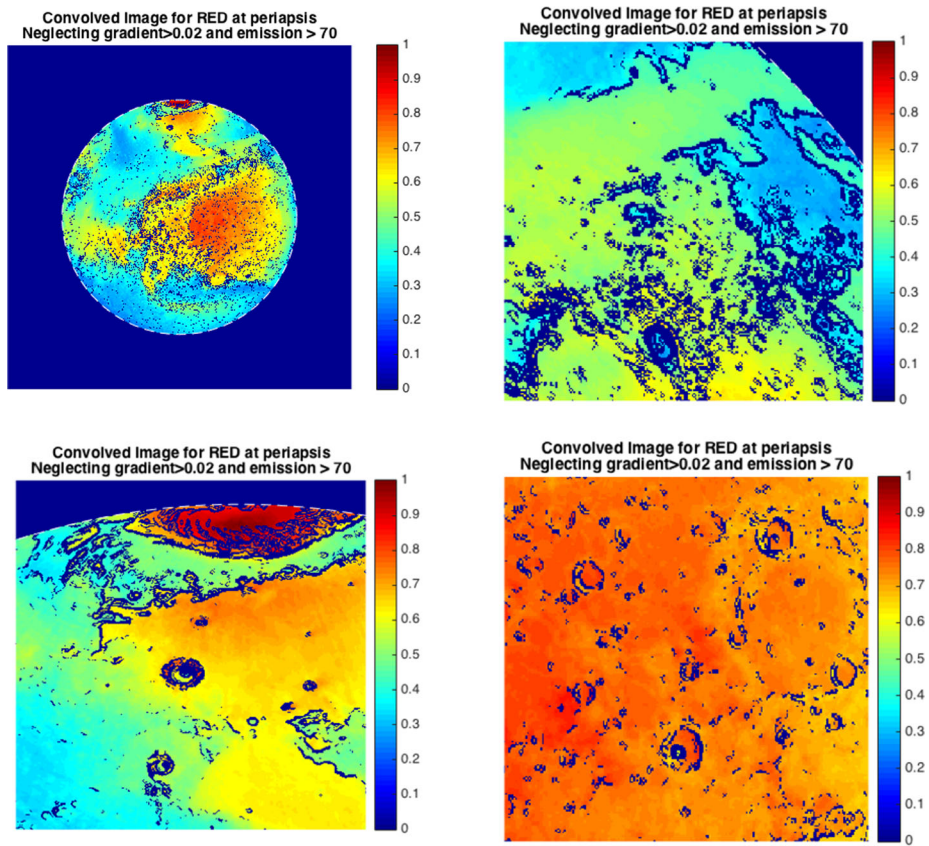
Fig. 30 Processed results from Fig. 26, setting pixels with local gradient > 0.02 to 0

FAD	Flight Activity Definition
FFT	Fast Fourier Transform
FITS	Flexible Image Transport System
FM	Flight Model
FOV	Field-of-View
FPGA	Field Programmable Gate Array
FSW	Flight SoftWare
FWHM	Full Width at Half Maximum
GN_2	Gaseous Nitrogen
HK	HouseKeeping [data]
HST	Hubble Space Telescope
IO	Input Output
IP	Intellectual Property
ISO	International Standard Organization
ITF	Instrument Team Facility
ITU	International Telecommunication Union

JMARS	JAVA Mission-planning and Analysis for Remote Sensing
JPEG	Joint Photographic Experts Group
JPL	Jet Propulsion Laboratory
LASP	Laboratory for Atmospheric and Space Physics
LDO	Low Drop Out
LED	Light Emitting Diode
LEOP	Launch and Early Operation Phase
LN_2	Liquid Nitrogen
LVDS	Low Voltage Differential Signal
MAGIC	MArs diGital Image Compression Board
MARCI	MARs Color Imager
MBRSC	Mohammed Bin Rashid Space Centre
MCS	Mars Climate Sounder
MEPAG	Mars Exploration Program Analysis Group
MLI	Multi-Layer Insulating
MOI	Mars Orbit Insertion
MOLD	Mission Operations Long Duration testing
MRO	Mars Reconnaissance Orbiter
MTF	Modulation Transfer Function
NASA	National Aeronautics and Space Administration
NIST	National Institute of Standards and Technology
OASIS-CC	Operations and Science Instrument Support - Command Control
OTF	Optical Transfer Function
POL	Point of load
PR	Public Relations
PRESTO	PoweR sErviceS elecTrOnics Board
PROM	Programmable Read Only Memory
PSF	Point Spread Function
QE	Quantum Efficiency
QL	Quick Look
RF	Radio Frequency
RMS	Root Mean Square
ROI	Region Of Interest
RSS	Residual Sum of Squares
S/C	SpaceCraft
SCI	Science [data]
SDC	Science Data Center
SDRAM	Synchronous Dynamic Random Access Memory
SEE	Single Event Effects
SEFI	Single Event Functional Interrupt
SEU	Single Event Upset
SNR	Signal to Noise Ratio

SRAM	Static Random Access Memory
TB	Thermal Balance testing
TDD	Test Driven Development
TVAC	Thermal Vacuum testing
TID	Total Ionizing Dose
UAESA	United Arab Emirates Space Agency
UTC	Universal Coordinated Time
UV	Ultraviolet
VIBE	Vibration testing
VIS	Visible
XOS	eXi Observation Strategy

Declarations

Compliance with Ethical Standards The authors have complied with the ethical standards of Space Science Reviews in preparing this manuscript and conducting any analysis described therein.

Conflict of Interest The authors declare that they have no conflict of interest.

Ethical approval The authors approve the ethical standards declaration above.

Informed consent All authors have been informed of and agreed to the submission of this manuscript.

References

P. Adamiec, J. Barbero, A.L. Moya, E. Cordero, Radiation tests on the COTS image sensor from CMOSIS, in *International Conference on Space Optics — ICSO 2018*, ed. by Z. Sodnik, N. Karafolas, B. Cugny. International Society for Optics and Photonics, SPIE, vol. 11180 (2019), pp. 2779–2786. https://doi.org/10.1117/12.2536197

H.E.S. Amiri, D. Brain, O. Sharaf, P. Withnell, M. McGrath, M. AlAwadhi, H. AlMatroushi, Z. AlShamsi, O. AlShehhi, M. Chaffin, J. Deighan, C. Edwards, N. Ferrington, B. Harter, G. Holsclaw, M. Kelley, D. Kubitschek, H. Landin, R. Lillis, M. Packard, J. Parker, E. Pilinski, B. Pramman, H. Reed, S. Ryan, C. Sanders, M. Smith, R. Wrigley, H. AlMazmi, N. AlMheiri, M. AlShamsi, E. AlTunaiji, K. Badri, P. Christensen, S. England, M. Fillingim, F. Forget, S.K. Jain, B.M. Jakosky, A. Jones, F. Lootah, J.G. Luhmann, M. Osterloo, M. Wolff, M. Yousuf, The emirates Mars mission. Space Sci. Rev. (2021), this journal

C.A. Barth, C.W. Hord, A.I. Stewart, A.L. Lane, M.L. Dick, G.P. Anderson, Mariner 9 ultraviolet spectrometer experiment: seasonal variation of ozone on Mars. Science **179**(4075), 795–796 (1973). https://doi.org/10.1126/science.179.4075.795

A. BenMoussa, S. Gissot, B. Giordanengo, G. Meynants, X. Wang, B. Wolfs, J. Bogaerts, U. Schühle, G. Berger, A. Gottwald, C. Laubis, U. Kroth, F. Scholze, A. Soltani, T. Saito, Irradiation damage tests on backside-illuminated cmos aps prototypes for the extreme ultraviolet imager on-board solar orbiter. IEEE Trans. Nucl. Sci. **60**(5), 3907–3914 (2013a)

A. BenMoussa, S. Gissot, U. Schühle, G. Del Zanna, F. Auchère, S. Mekaoui, A.R. Jones, D. Walton, C.J. Eyles, G. Thuillier, D. Seaton, I.E. Dammasch, G. Cessateur, M. Meftah, V. Andretta, D. Berghmans, D. Bewsher, D. Bolsée, L. Bradley, D.S. Brown, P.C. Chamberlin, S. Dewitte, L.V. Didkovsky, M. Dominique, F.G. Eparvier, T. Foujols, D. Gillotay, B. Giordanengo, J.P. Halain, R.A. Hock, A. Irbah, C. Jeppesen, D.L. Judge, M. Kretzschmar, D.R. McMullin, B. Nicula, W. Schmutz, G. Ucker, S. Wieman, D. Woodraska, T.N. Woods, On-orbit degradation of solar instruments. Sol. Phys. **288**(1), 389–434 (2013b). https://doi.org/10.1007/s11207-013-0290-z. 1304.5488

L. Bradley, B. Sipőcz, T. Robitaille, E. Tollerud, Z. Vinícius, C. Deil, K. Barbary, T.J. Wilson, I. Busko, H.M. Günther, M. Cara, S. Conseil, A. Bostroem, M.l Droettboom, E.M. Bray, L.A. Bratholm, P.L. Lim, G. Barentsen, M. Craig, S. Pascual, G. Perren, J. Greco, A. Donath, M. de Val-Borro, W. Kerzendorf, Y.P. Bach, B.A. Weaver, F. D'Eugenio, H. Souchereau, L. Ferreira, astropy/photutils: 1.0.0 (2020). https://doi.org/10.5281/zenodo.4044744

B.A. Cantor, P.B. James, W.M. Calvin, MARCI and MOC observations of the atmosphere and surface cap in the North polar region of Mars. Icarus **208**(1), 61–81 (2010). https://doi.org/10.1016/j.icarus.2010.01.032

P.R. Christensen, Martian dust mantling and surface composition: interpretation of thermophysical properties. J. Geophys. Res. **87**, 9985–9998 (1982). https://doi.org/10.1029/JB087iB12p09985

P.R. Christensen, E. Engle, S. Anwar, S. Dickenshied, D. Noss, N. Gorelick, M. Weiss-Malik, JMARS - a planetary GIS, in *AGU Fall Meeting Abstracts*, vol. 2009 (2009), pp. IN22A–06

R.T. Clancy, M.J. Wolff, B.A. Whitney, B.A. Cantor, M.D. Smith, Mars equatorial mesospheric clouds: global occurrence and physical properties from mars global surveyor thermal emission spectrometer and Mars orbiter camera limb observations. J. Geophys. Res., Planets **112**(E4), E04004 (2007). https://doi.org/10.1029/2006JE002805

R.T. Clancy, M.J. Wolff, F. Lefèvre, B.A. Cantor, M.C. Malin, M.D. Smith, Daily global mapping of Mars ozone column abundances with MARCI UV band imaging. Icarus **266**, 112–133 (2016). https://doi.org/10.1016/j.icarus.2015.11.016

R.T. Clancy, F. Montmessin, J. Benson, F. Daerden, A. Colaprete, M.J. Wolff, *Mars Clouds* (Cambridge University Press, Cambridge, 2017), pp. 42–75. https://doi.org/10.1017/9781139060172.005

Community Sensor Model Working Group, Frame sensor model metadata profile supporting precise geopositioning version 1.0. CSMWG information guidance document. National Geospatial-Intelligence Agency & Air Force Aeronautical Systems Center (2007)

Corning, Corning Glass Data (2020). https://www.corning.com/worldwide/en/products/advanced-optics/product-materials/specialty-glass-and-glass-ceramics/ophthalmic-glass/glass-products-data-sheets.html

C. Edwards, K. Nowicki, P. Christensen, J. Hill, N. Gorelick, K. Murray, Mosaicking of global planetary image datasets: 1. Techniques and data processing for thermal emission imaging system (themis) multispectral data. J. Geophys. Res. **116**, E10008 (2011). https://doi.org/10.1029/2010JE003755

J. Fowler, M. Litorja, Geometric area measurements of circular apertures for radiometry at NIST. Metrologia **40**(1), S9–S12 (2003)

B.M. Jakosky, M.T. Mellon, H.H. Kieffer, P.R. Christensen, E.S. Varnes, S.W. Lee, The thermal inertia of Mars from the Mars global surveyor thermal emission spectrometer. J. Geophys. Res. **105**(E4), 9643–9652 (2000). https://doi.org/10.1029/1999JE001088

P.B. James, J.F. Bell, R.T. Clancy, S.W. Lee, L.J. Martin, M.J. Wolff, Global imaging of Mars by Hubble space telescope during the 1995 opposition. J. Geophys. Res. **101**(E8), 18,883–18,890 (1996). https://doi.org/10.1029/96JE01605

M.A. Kahre, J.R. Murphy, C.E. Newman, R.J. Wilson, B.A. Cantor, M.T. Lemmon, M.J. Wolff, *The Mars Dust Cycle* (Cambridge University Press, Cambridge, 2017), pp. 229–294. https://doi.org/10.1017/9781139060172.010

H.H. Kieffer, S.C. Chase Jr., E. Miner, G. Münch, G. Neugebauer, Preliminary report on infrared radiometric measurements from the mariner 9 spacecraft. J. Geophys. Res. (1896-1977) **78**(20), 4291–4312 (1973). https://doi.org/10.1029/JB078i020p04291

M.C. Malin, W.M. Calvin, B.A. Cantor, R.T. Clancy, R.M. Haberle, P.B. James, P.C. Thomas, M.J. Wolff, J.F. Bell, S.W. Lee, Climate, weather, and North polar observations from the Mars Reconnaissance Orbiter Mars Color Imager. Icarus **194**(2), 501–512 (2008). https://doi.org/10.1016/j.icarus.2007.10.016

D.J. McCleese, J.T. Schofield, F.W. Taylor, S.B. Calcutt, M.C. Foote, D.M. Kass, C.B. Leovy, D.A. Paige, P.L. Read, R.W. Zurek, Mars climate sounder: an investigation of thermal and water vapor structure, dust and condensate distributions in the atmosphere, and energy balance of the polar regions. J. Geophys. Res., Planets **112**(E5), E05S06 (2007). https://doi.org/10.1029/2006JE002790

W.E. McClintock, D.W. Rusch, G.E. Thomas, A.W. Merkel, M.R. Lankton, V.A. Drake, S.M. Bailey, J.M. Russell III, The cloud imaging and particle size experiment on the aeronomy of ice in the mesosphere mission: instrument concept, design, calibration, and on-orbit performance. J. Atmos. Sol.-Terr. Phys. **71**(3–4), 340–355 (2009). https://doi.org/10.1016/j.jastp.2008.10.011

MEPAG, Mars scientific goals, objectives, investigations and priorities, in *Mars Exploration Program Analysis Group (MEPAG)*, ed. by D. Banfield (2020), pp. 1–89. https://mepag.jpl.nasa.gov/reports.cfm

NIST (2020a). https://www.nist.gov/programs-projects/primary-optical-watt-radiometer-powr

NIST (2020b). https://www.nist.gov/programs-projects/spectral-irradiance-and-radiance-responsivity-calibrations-using-uniform-sources

Schott, Schott Glass Data (2020). https://www.us.schott.com/advanced_optics/english/products/optical-materials/optical-glass/optical-glass/index.html

L. Shing, C. Edwards, D. Mathur, G. Vasudevan, M. Shaw, C. Nwachuku, GOES-R SUVI EUV flatfields generated using boustrophedon scans, in *AGU Fall Meeting Abstracts*, vol. 2017 (2017), pp. SH21A–2642

D.A. Turnshek, R.C. Bohlin, R.L. Williamson II, O.L. Lupie, J. Koornneef, D.H. Morgan, An Atlas of Hubble Space Telescope photometric, spectrophotometric, and polarimetric calibration objects. Astron. J. **99**, 1243–1261 (1990). https://doi.org/10.1086/115413

M. Weinberger, G. Seroussi, G. Sapiro, The loco-i lossless image compression algorithm: principles and standardization into jpeg-ls. IEEE Trans. Image Process. **9**, 8:1309–1324 (2000), originally as, Hewlett-Packard Laboratories Technical Report No. HPL-98-193R1, 1998, revised October 1999

M.J. Wolff, P.B. James, R. Todd Clancy, S.W. Lee, Hubble Space Telescope observations of the Martian aphelion cloud belt prior to the Pathfinder mission: seasonal and interannual variations. J. Geophys. Res. **104**(E4), 9027–9042 (1999). https://doi.org/10.1029/98JE01967

M.J. Wolff, M. Lopéz-Valverde, J.B. Madeleine, R.J. Wilson, M.D. Smith, T. Fouchet, G.T. Delory, *Radiative Processes: Techniques and Applications* (Cambridge University Press, Cambridge, 2017), pp. 76–105. https://doi.org/10.1017/9781139060172.006

M.J. Wolff, R.T. Clancy, M.A. Kahre, R.M. Haberle, F. Forget, B.A. Cantor, M.C. Malin, Mapping water ice clouds on Mars with MRO/MARCI. Icarus **332**, 24–49 (2019). https://doi.org/10.1016/j.icarus.2019.05.041

Authors and Affiliations

A.R. Jones[1] · M. Wolff[2] · M. Alshamsi[3] · M. Osterloo[2] · P. Bay[1] · N. Brennan[1] · K. Bryant[1] · Z. Castleman[1] · A. Curtin[1] · E. DeVito[1] · V.A. Drake[1] · D. Ebuen[1] · J. Espejo[1] · J. Farren[1] · B. Fenton[1] · C. Fisher[1] · M. Fisher[1] · K. Fortier[1] · S. Gerwig[1] · B. Heberlein[1] · C. Jeppesen[1] · M.A. Khoory[3] · S. Knappmiller[1] · J. Knavel[1] · K. Koski[1] · K. Looney[1] · P. Lujan[1] · M. Miller[1] · G. Newcomb[1] · G. Otzinger[1] · H. Passe[1] · E. Pilinski[1] · H. Reed[1] · R. Shuping[2] · P. Sicken[1] · D. Summers[1] · S. Wade[1] · L. Walton[1] · J.L. Yaptengco[1]

✉ A.R. Jones
andrew.jones@lasp.colorado.edu

M. Wolff
mjwolff@spacescience.org

M. Alshamsi
Mariam.AlShamsi@mbrsc.ae

[1]   LASP, University of Colorado, Boulder, 3665 Discovery Drive, Boulder, CO 80303, USA

[2]   Space Science Institute, Boulder, CO 80301, USA

[3]   Mohammed bin Rashid Space Centre, P.O. Box: 211833, Dubai, UAE